

# Chimica Techno Acta



ISSN 2411-1414 (online)

<http://chimicatechnoacta.ru>

September 2021 | Volume 8 | Issue 3



Ural Federal  
University

named after the first President  
of Russia B.N.Yeltsin

## Chimica Techno Acta (eISSN 2411-1414)

Scientific and Technical Open Access Journal  
Distributed for free  
Established in 2014/Published four times per year

2021 | Vol. 8 | No. 3

This issue was published on 30.09.2021

**Founded and published by Ural Federal University**

19 Mira St., Ekaterinburg, 620002, Russia

## Editorial Board

### Editor-in-Chief

Dmitry A. Medvedev, Institute of High Temperature Electrochemistry, Ekaterinburg,  
Russia

### Editors

Andrey Yu. Zuev, Ural Federal University, Ekaterinburg, Russia  
Evgeny V. Antipov, Moscow State University, Moscow, Russia  
Vladimir A. Cherepanov, Ural Federal University, Ekaterinburg, Russia  
Antoine Maignan, CRISMAT Laboratory, ENSICAEN, Caen, France  
Ekaterina Kozlova, Boreskov Institute of Catalysis, Novosibirsk, Russia  
Panagiotis Tsiakaras, University of Thessaly Greece, Greece  
Shuqin Song, Sun Yat-sen University, Guangzhou, China  
Yi Wang, Sun Yat-sen University, Guangzhou, China  
Zhi-Jin Fan, Nankai University, Tianjin, China  
Victor V. Gusarov, Ioffe Institute, Saint Petersburg, Russia  
Vladislav V. Kharton, Institute of Solid State Physics, Chernogolovka, Russia  
Alexander A. Mikhailovsky, University of California, Santa Barbara, United States  
Vladimir V. Pankov, Belarusian State University, Minsk, Belarus  
Sougata Santra, Ural Federal University, Ekaterinburg, Russia  
Nadezda V. Tarakina, Fritz Haber Institute, Berlin, Germany  
Grigory V. Zyryanov, Ural Federal University, Ekaterinburg, Russia

### Managing Editor

Tatiana A. Pospelova (Ekaterinburg, Russia)

### Copyeditor

Vladimir V. Sereda (Ekaterinburg, Russia)

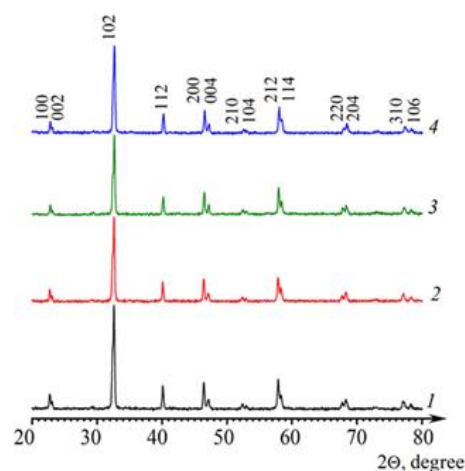
## Contents

### 20218301

ARTICLE / Regular Issue

A.I. Klyndyuk, Ya.Yu. Zhuravleva, N.N. Gundilovich

**Crystal structure, thermal and electrotransport properties of  $\text{NdBa}_{1-x}\text{Sr}_x\text{FeCo}_{0.5}\text{Cu}_{0.5}\text{O}_{5+\delta}$  ( $0.02 \leq x \leq 0.20$ ) solid solutions**

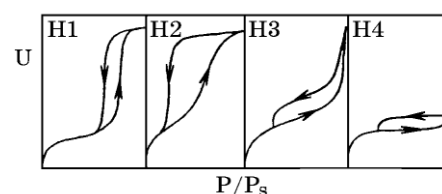


### 20218302

ARTICLE / Regular Issue

S. Tokmeilova, E.V. Maraeva

**Overview of sorption analysis capabilities for meso- and microporous zeolites nanomaterials**

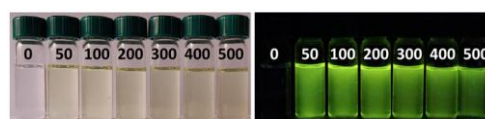


### 20218303

ARTICLE / Regular Issue

Alexander K. Eltyshev, Nataliya P. Belskaya

**Sensitivity of the phenoxy derivatives of 2,4-dihydro-5H-[1,2,3]triazolo[4,5-d]pyrimidin-5-ones to acidic and basic stimuli**

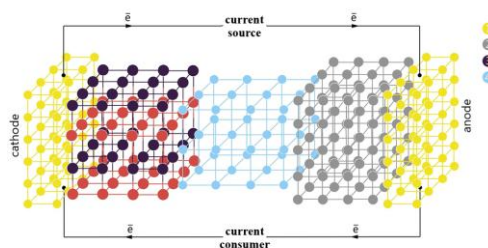


### 20218304

REVIEW / Regular Issue

Semyon Bachinin, Venera Gilemkhanova,  
 Maria Timofeeva, Yuliya Kenzhebayeva, Andrei Yankin,  
 Valentin A. Milichko

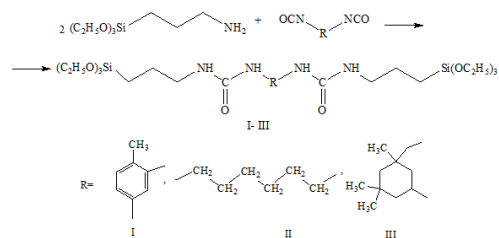
**Metal-Organic Frameworks for Metal-Ion Batteries: Towards Scalability**



## 20218305

LETTER / Regular Issue

K.Yu. Ivanova, M.V. Kuzmin, L.G. Rogozhina,  
A.O. Patianova, V.L. Semenov, R.I. Alexandrov



### Synthesis and research of polyfunctional silylureas used in electric deposition of tin-indium alloy

## 20218306

ARTICLE / Regular Issue

A.S. Lyutina, A.A. Kataev, A.V. Rudenko,  
O.Yu. Tkacheva



### Effect of Al<sub>2</sub>O<sub>3</sub> and CaF<sub>2</sub> additives on the viscosity of conventional cryolite melts

# Crystal structure, thermal and electrotransport properties of $\text{NdBa}_{1-x}\text{Sr}_x\text{FeCo}_{0.5}\text{Cu}_{0.5}\text{O}_{5+\delta}$ ( $0.02 \leq x \leq 0.20$ ) solid solutions



A.I. Klyndyuk\*, Ya.Yu. Zhuravleva, N.N. Gundilovich

Belarus State Technological University, 13a Sverdlova str., Minsk, 220006, Belarus Republic

\* Corresponding author: [klyndyuk@belstu.by](mailto:klyndyuk@belstu.by)

This article belongs to the regular issue.

© 2021, The Authors. This article is published in open access form under the terms and conditions of the Creative Commons Attribution (CC BY) license (<http://creativecommons.org/licenses/by/4.0/>).

## Abstract

Using solid-state reactions method, the solid solutions of layered oxygen-deficient perovskites  $\text{NdBa}_{1-x}\text{Sr}_x\text{FeCo}_{0.5}\text{Cu}_{0.5}\text{O}_{5+\delta}$  ( $0.02 \leq x \leq 0.20$ ) were prepared; their crystal structure, thermal stability, thermal expansion, electrical conductivity and thermopower were studied. It was found that  $\text{NdBa}_{1-x}\text{Sr}_x\text{FeCo}_{0.5}\text{Cu}_{0.5}\text{O}_{5+\delta}$  phases crystallize in tetragonal syngony (space group  $P4/mmm$ ) and are  $p$ -type semiconductors, whose conductivity character at high temperatures changed to the metallic one due to evolution from the samples of so-called weakly-bonded oxygen. Partial substitution of barium by strontium in  $\text{NdBaFeCo}_{0.5}\text{Cu}_{0.5}\text{O}_{5+\delta}$  leads to the small decreasing of unit cell parameters, thermal stability and thermopower of  $\text{NdBa}_{1-x}\text{Sr}_x\text{FeCo}_{0.5}\text{Cu}_{0.5}\text{O}_{5+\delta}$  solid solutions, increasing of their electrical conductivity values and slightly affects their linear thermal expansion coefficient and activation energy of electrical transport values.

## Keywords

layered perovskites  
thermal stability  
thermal expansion  
electrical conductivity  
thermopower

Received: 02.06.2021

Revised: 01.07.2021

Accepted: 08.07.2021

Available online: 08.07.2021

## 1. Introduction

Layered oxygen-deficient double perovskites of  $\text{LnBaMe}'\text{Me}''\text{O}_{5+\delta}$  ( $\text{Ln} - \text{Y}$ , rare-earth element (REE),  $\text{Me}'$ ,  $\text{Me}'' - 3d$ -metal) have a complex of unique properties, including large values of electrical conductivity and thermopower, and contain in their structure labile oxygen, so they may be used as functional materials for different purposes: high-temperature oxide thermoelectrics, electrode materials for solid-oxide fuel cells (SOFC), materials for working elements of semiconducting chemical gas sensors, catalysts of hydrocarbons oxidation, etc. [1–6].

$\text{LnBaCo}_2\text{O}_{5+\delta}$  phases demonstrate high electrochemical performance in oxygen reduction reaction (ORR) [4–8], but values of their linear thermal expansion coefficient (TEC,  $\alpha$ ) are too large (circa  $(15\text{--}29) \cdot 10^{-6} \text{ K}^{-1}$  [7–9]) in comparison to the TEC of commonly used in SOFC zirconia, ceria, or perovskite-like based solid electrolytes, which are equal to  $(10\text{--}11) \cdot 10^{-6} \text{ K}^{-1}$ ,  $(12\text{--}13) \cdot 10^{-6}$ , and  $(10\text{--}13) \cdot 10^{-6} \text{ K}^{-1}$  respectively [10], which limits the practical implementation of these phases as cathode materials in SOFC.

Many studies [8,9,11–18] have demonstrated that partial substitution in  $\text{LnBaCo}_2\text{O}_{5+\delta}$  of cobalt by other  $3d$ -metal or barium by strontium essentially improves electrochemical performance of solid solutions forming at such substitution and reduces their TEC value. So, partial substitution of cobalt by iron in  $\text{LnBaCo}_2\text{O}_{5+\delta}$  ( $\text{Ln} - \text{Pr}$ ,  $\text{Nd}$ ) leads to the reducing of TEC and polarization resistance of materials forming at this substitution and also improves their long-term stability at implementation as cathode materials of SOFC [12,13,15]. Doping of barium by strontium and of cobalt by copper or iron in  $\text{YBaCo}_2\text{O}_{5+\delta}$  lead to the reducing of TEC of forming solid solutions, improving of their structural stability and electrochemical performance [9,16].

So, obtaining and studying of solid solutions, including complex substituted ones, on the basis of layered oxygen-deficient double perovskites is an actual task, having scientific and practical interest.

In this work we studied the effect of partial substitution of barium by strontium in  $\text{NdBaFeCo}_{0.5}\text{Cu}_{0.5}\text{O}_{5+\delta}$  on the crystal structure, thermal and electrotransport properties of  $\text{NdBa}_{1-x}\text{Sr}_x\text{FeCo}_{0.5}\text{Cu}_{0.5}\text{O}_{5+\delta}$  solid solutions as perspective cathode materials for intermediate-temperature SOFC.

## 2. Experimental

Ceramic samples of  $\text{NdBa}_{1-x}\text{Sr}_x\text{FeCo}_{0.5}\text{Cu}_{0.5}\text{O}_{5+\delta}$  ( $x = 0.02, 0.05, 0.10, \text{ and } 0.20$ ) solid solutions were prepared by means of solid-state reactions method from  $\text{Nd}_2\text{O}_3$  (NO-L),  $\text{BaCO}_3$  (pure),  $\text{SrCO}_3$  (pure),  $\text{Fe}_2\text{O}_3$  (super pure 2-4),  $\text{Co}_3\text{O}_4$  (pure), and  $\text{CuO}$  (pure for analysis) in air at temperature of 1173 K within 40 h with consequent sintering during 9–18 h in air at temperatures of 1223–1273 K according to the methods, described in [19,20].

Identification of the samples and determination of their lattice constants was performed by means of X-ray diffraction analysis (XRD) (X-ray diffractometer Bruker D8 Advance XRD, Cu  $K\alpha$ -radiation). IR-absorption spectra of powders were recorded in the mixtures with KBr within 300–1500  $\text{cm}^{-1}$  (ThermoNicolet Nexus Fourier-Transform Infrared Spectrometer). Apparent (effective) density of the sintered ceramics ( $\rho_{\text{eff}}$ ) was determined from the mass and dimensions of the samples, and their porosity ( $\Pi$ ) was calculated using Eq. (1):

$$\Pi = (1 - \rho_{\text{eff}}/\rho_{\text{XRD}}) \cdot 100\%, \quad (1)$$

where  $\rho_{\text{XRD}}$  – X-ray density of the samples.

Thermal stability of the powdered samples was studied by means of thermoanalytical system of TGA/DSC-1/1600 HF in air within 300–1100 K temperature interval. Thermal expansion of the sintered ceramics was investigated using DIL 402 PC quartz dilatometer in air within temperature interval of 300–1100 K [21]. Electrical conductivity and thermopower of  $\text{NdBa}_{1-x}\text{Sr}_x\text{FeCo}_{0.5}\text{Cu}_{0.5}\text{O}_{5+\delta}$  solid solutions were studied in air within 300–1100 K according to the methods, described in detail in [20]. Values of TEC and apparent activation energies of electrical conductivity ( $E_A$ ) and thermopower ( $E_S$ ) were calculated from the linear parts of

$\Delta l/l_0 = f(T)$ ,  $\ln(\sigma \cdot T) = f(1/T)$ , and  $S = f(1/T)$  dependences, respectively.

## 3. Results and Discussion

After final stage of the synthesis, all the samples of the  $\text{NdBa}_{1-x}\text{Sr}_x\text{FeCo}_{0.5}\text{Cu}_{0.5}\text{O}_{5+\delta}$  solid solutions were single phase, within XRD accuracy (Fig. 1a), and had a structure of tetragonally distorted double perovskite of  $\text{YBaCuFeO}_5$  type ( $a \approx a_p, c \approx 2a_p$ ) [1], and their reflections were indexed in the framework of the  $P4/mmm$  space group with unit cell parameters of  $a = 3.903\text{--}3.914 \text{ \AA}$  and  $c = 7.707\text{--}7.715 \text{ \AA}$  (Table 1).

As can be seen from the Table 1, increasing of the substitution degree of larger  $\text{Ba}^{2+}$  ion by smaller  $\text{Sr}^{2+}$  one (for C.N. = 12  $R(\text{Ba}^{2+}) = 1.60 \text{ \AA}$ ,  $R(\text{Sr}^{2+}) = 1.44 \text{ \AA}$  [22]) leads to the decreasing of the size of the unit cell of the  $\text{NdBa}_{1-x}\text{Sr}_x\text{FeCo}_{0.5}\text{Cu}_{0.5}\text{O}_{5+\delta}$  phases. Porosity of the sintered ceramics enlarged at  $x$  increasing (Table 1), which let us conclude that partial substitution of barium by strontium in  $\text{NdBaFeCo}_{0.5}\text{Cu}_{0.5}\text{O}_{5+\delta}$  slightly reduces sinterability of this perovskite.

On the IR-absorption spectra of the samples were detected some absorption bands with extrema at 351–353  $\text{cm}^{-1}$  ( $\nu_1$ ), 467–470  $\text{cm}^{-1}$  ( $\nu_2$ ), 576–582  $\text{cm}^{-1}$  ( $\nu_3$ ), and 660–665  $\text{cm}^{-1}$  ( $\nu_4$ ) (Fig. 1b), which were attributed, according to [23], to the stretching ( $\nu_3, \nu_4$ ) and bending vibrations ( $\nu_1$ ) of the (Fe,Co,Cu)–O–(Fe,Co,Cu) bonds in the [(Fe,Co,Cu)O<sub>2</sub>] basal planes ( $\nu_1, \nu_3$ ), as well as stretching vibrations of apical oxygen of (Fe,Co,Cu)–O–(Fe,Co,Cu) bonds along  $c$  axis ( $\nu_4$ ) in the structure of  $\text{NdBa}_{1-x}\text{Sr}_x\text{FeCo}_{0.5}\text{Cu}_{0.5}\text{O}_{5+\delta}$  phases. At  $x$  increasing the  $\nu_3$  and  $\nu_4$  bands shifted to the larger values,

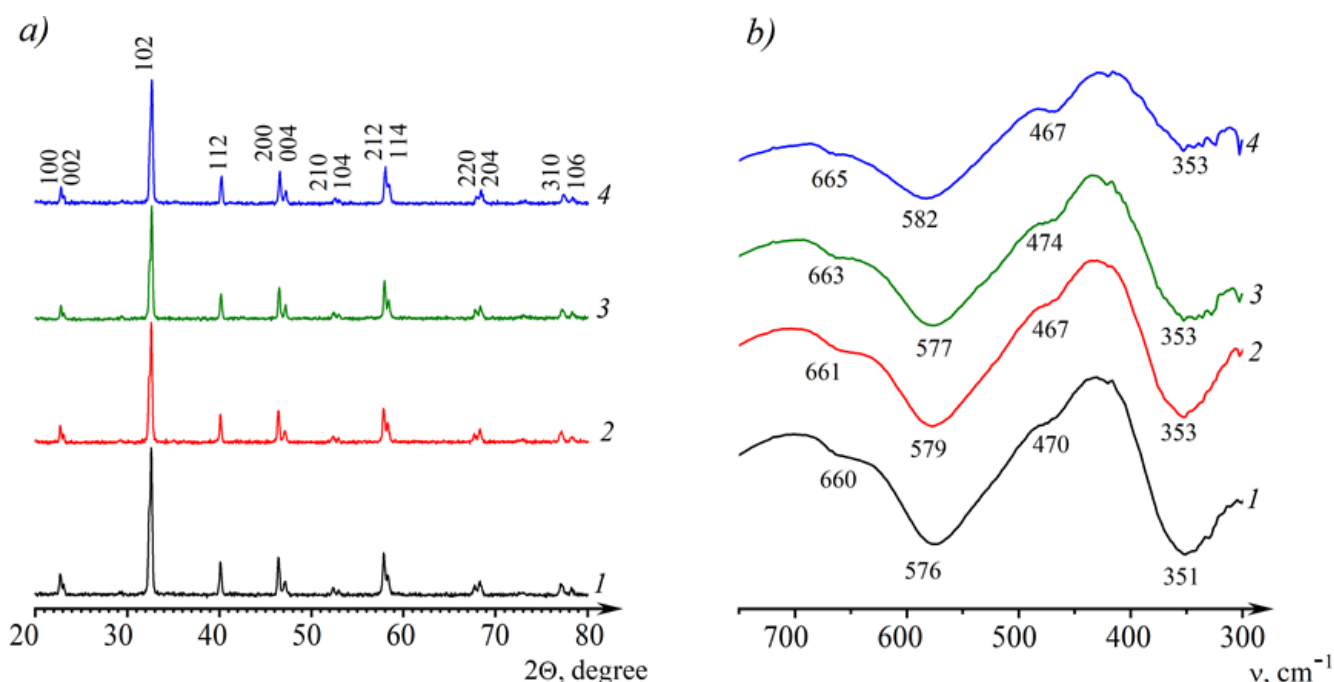


**Fig. 1** X-ray powder diffractograms (a) and IR-absorption spectra (b) of  $\text{NdBa}_{1-x}\text{Sr}_x\text{FeCo}_{0.5}\text{Cu}_{0.5}\text{O}_{5+\delta}$  solid solutions:  $x = 0.02$  (1);  $0.05$  (2);  $0.10$  (3);  $0.20$  (4)

**Table 1** The unit cell parameters (*a*, *c*, *c/2a*, *V*), effective density ( $\rho_{eff}$ ) and porosity ( $\Pi$ ) of NdBa<sub>1-x</sub>Sr<sub>x</sub>FeCo<sub>0.5</sub>Cu<sub>0.5</sub>O<sub>5+δ</sub> layered perovskites finally sintered at 1273 K

<i>x</i>	<i>a</i> , Å	<i>c</i> , Å	<i>c/2a</i> , Å	<i>V</i> , Å <sup>3</sup>	$\rho_{eff}$ , g/cm <sup>3</sup>	$\Pi$ , %
0.02	3.913(1)	7.715(1)	0.9860	118.1(1)	5.54	10
0.05	3.914(1)	7.711(1)	0.9851	118.1(1)	5.62	8
0.10	3.911(2)	7.707(2)	0.9853	117.9(1)	5.54	12
0.20	3.903(1)	7.708(1)	0.9876	117.5(1)	4.84	21

which pointed out to increasing of energy of metal–oxygen interactions in the crystal structure of these phases. Results of IR-absorption spectroscopy correlate with the XRD results, showing that increasing of substitution degree of barium by strontium in NdBa<sub>1-x</sub>Sr<sub>x</sub>FeCo<sub>0.5</sub>Cu<sub>0.5</sub>O<sub>5+δ</sub> solid solutions leads to the shrinking of their unit cell.

According to the results of thermal analysis, near the room temperature all the samples were thermally stable, but, beginning from the temperatures of 623–663 K (*T<sub>b</sub>*) the small mass loss (0.6–0.8%) was detected (Fig. 2a), which took place due to the evolution of the labile (weakly-bonded) oxygen from the samples into environment [24]. Values of *T<sub>b</sub>* decreased at *x* increasing (Fig. 2c, Table 2), which indicated increasing of mobility of weakly-bonded oxygen in the structure of NdBa<sub>1-x</sub>Sr<sub>x</sub>FeCo<sub>0.5</sub>Cu<sub>0.5</sub>O<sub>5+δ</sub> solid solutions at increasing of substitution degree of barium by strontium. On the temperature dependences of the relative elongation ( $\Delta l/l_0$ ) of materials studied an anomaly in a kink near *T<sub>k</sub>* = 640–680 K accompanied by the increase the TEC value was detected (Fig. 2b, Table 2), which took place due to the rearrangement of oxygen sublattice of the samples with consequent evolution of oxygen from them in air [24]. TEC values of ceramics in high-temperature region ( $\alpha_{HT}$ , *T* > *T<sub>k</sub>*) were 15–24% larger than in the low-temperature

one ( $\alpha_{LT}$ , *T* < *T<sub>k</sub>*) (Table 3). Values of TEC of NdBa<sub>1-x</sub>Sr<sub>x</sub>FeCo<sub>0.5</sub>Cu<sub>0.5</sub>O<sub>5+δ</sub> solid solutions in both temperature regions slightly varied but temperature of anomaly (*T<sub>k</sub>*) essentially decreased (Fig. 2d) at *x* increasing.

As can be seen from the data given in the Fig. 3a,b, materials studied are *p*-type (*S* > *o*) semiconductors ( $\partial\sigma/\partial T > 0$ ). Their conductivity character at high temperatures (*T* > *T<sub>max</sub>*) changed to the metallic one ( $\partial\sigma/\partial T < 0$ ), which was accompanied by the change of the sign of the  $\partial S/\partial T$  derivative ( $\partial S/\partial T < 0$  at *T* < *T<sub>min</sub>* and  $\partial S/\partial T > 0$  at *T* > *T<sub>min</sub>*). Observed anomalies of electrotransport properties of NdBa<sub>1-x</sub>Sr<sub>x</sub>FeCo<sub>0.5</sub>Cu<sub>0.5</sub>O<sub>5+δ</sub> phases as well as described earlier anomaly of thermal expansion were due to the evolution of the weakly-bonded oxygen from the samples [24]. Note that temperatures of  $\sigma$  and *S* anomalies, *T<sub>max</sub>* and *T<sub>min</sub>* respectively, at *x* increasing shifted to the smaller temperatures (Fig. 3c,d, Table 2) like *T<sub>b</sub>* and *T<sub>k</sub>* temperatures. It is interesting that values of *T<sub>b</sub>*, *T<sub>k</sub>* and *T<sub>min</sub>* temperatures were rather close to each other, but *T<sub>max</sub>* value was essentially larger (Table 2, Figs. 2c,d, 3c,d). Values of all critical temperatures (*T<sub>cr</sub>*: *T<sub>b</sub>*, *T<sub>k</sub>*, *T<sub>max</sub>*, and *T<sub>min</sub>*) decrease at increasing of strontium content in the NdBa<sub>1-x</sub>Sr<sub>x</sub>FeCo<sub>0.5</sub>Cu<sub>0.5</sub>O<sub>5+δ</sub> solid solutions, hereby dependence *T<sub>cr</sub>* = *f*(*x*) was almost linear for *T<sub>k</sub>*, under-linear for *T<sub>b</sub>* and *T<sub>min</sub>*, and over-linear for *T<sub>max</sub>* increased despite of the

**Table 2** Values of critical temperatures (*T<sub>b</sub>*, *T<sub>k</sub>*, *T<sub>max</sub>*, and *T<sub>min</sub>*) of NdBa<sub>1-x</sub>Sr<sub>x</sub>FeCo<sub>0.5</sub>Cu<sub>0.5</sub>O<sub>5+δ</sub> ceramics

<i>x</i>	<i>T<sub>b</sub></i> , K	<i>T<sub>k</sub></i> , K	<i>T<sub>max</sub></i> , K	<i>T<sub>min</sub></i> , K
0.02	663	680	734	685
0.05	631	670	733	665
0.10	631	660	730	650
0.20	623	640	709	650

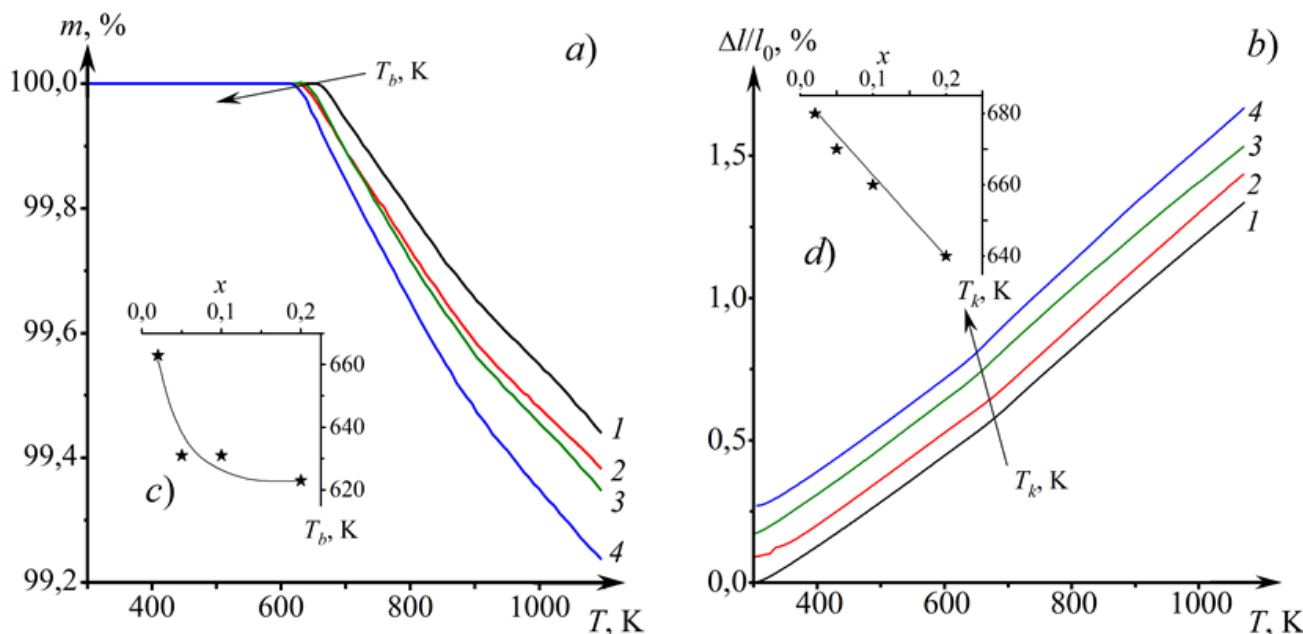


**Fig. 2** Temperature dependences of mass loss (a) and relative elongation (b) of NdBa<sub>1-x</sub>Sr<sub>x</sub>FeCo<sub>0.5</sub>Cu<sub>0.5</sub>O<sub>5+δ</sub> samples: *x* = 0.02 (1); 0.05 (2); 0.10 (3); 0.20 (4). Dilatometric curves are shifted from each other by 0.1% for the clarity of presentation. Insets show concentration dependences of temperatures of mass loss onset (c) and kink of the  $\Delta l/l_0 = f(T)$  dependences (d)

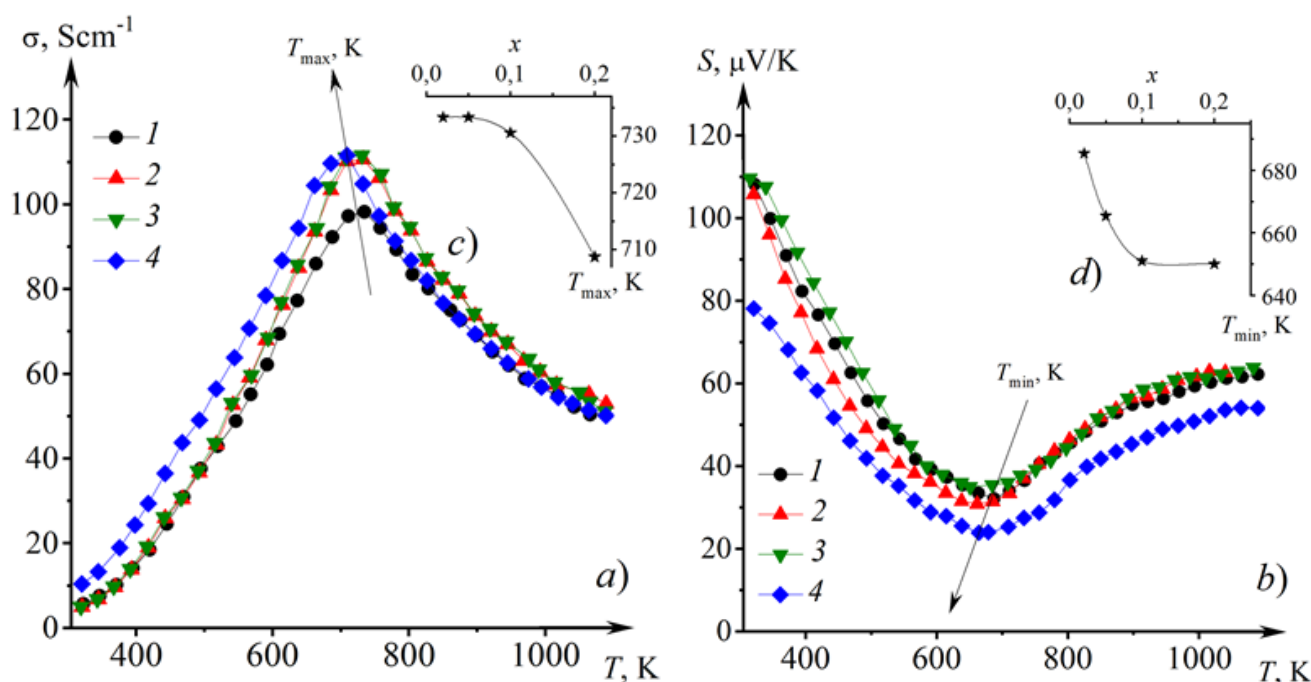


**Fig. 3** Temperature dependences of electrical conductivity (a) and thermo-EMF coefficient (b) of  $\text{NdBa}_{1-x}\text{Sr}_x\text{FeCo}_{0.5}\text{Cu}_{0.5}\text{O}_{5+\delta}$  sintered ceramics:  $x = 0.02$  (1);  $0.05$  (2);  $0.10$  (3);  $0.20$  (4). Insets shows concentration dependences of temperatures of maximum on the  $\sigma = f(T)$  dependences (c) and minimum of the  $S = f(T)$  dependences (d)

fact that porosity of the samples enlarged at increasing of strontium content (Table 1). So, our results show that partial substitution of barium by strontium in  $\text{NdBaFeCo}_{0.5}\text{Cu}_{0.5}\text{O}_{5+\delta}$  is an effective way to increase its electrical conductivity.

Layered oxygen-deficient double perovskites  $\text{LnBaMe}'\text{Me}''\text{O}_{5+\delta}$  possess polaronic character of charge transfer [1,19,24], and temperature dependences of their electrical conductivity and thermopower obey Eqs. (2-3)

$$\sigma = (A/T) \cdot \exp(-E_A/kT), \tag{2}$$

$$S = (k/e) \cdot (-E_S/kT + B), \tag{3}$$

where  $E_A = E_S + E_m$  and  $E_S$  - activation energies of electrical conductivity and thermopower respectively,  $E_S$  is also activation energy of charge carriers - polarons, and  $E_m$  is energy of their transfer [25].

As can be seen from the data given in the Table 3, values of energies of activation of electrical transport, in the whole, slightly varied at varying strontium content in the samples. Comparing obtained in this work results with the data of [24], where for  $\text{NdBaFeCo}_{0.5}\text{Cu}_{0.5}\text{O}_{5+\delta}$  layered perovskite was found that  $E_A = 0.245$  eV,  $E_S = 0.048$  eV, and  $E_m = 0.200$  eV, we can conclude that partial substitution

of barium by strontium in this parent phase does not affect practically the value of activation energy of charge carriers - polarons, but results in essential reducing of transfer energy of charge carriers.

### 4. Conclusions

By means of solid-state reactions method the ceramic samples of  $\text{NdBa}_{1-x}\text{Sr}_x\text{FeCo}_{0.5}\text{Cu}_{0.5}\text{O}_{5+\delta}$  ( $x = 0.02, 0.05, 0.10,$  and  $0.20$ ) solid solutions were prepared, and their crystal structure and physico-chemical properties were studied. It was found that obtained materials had tetragonal structure, whose unit cell parameters slightly depend on their cationic composition, and are p-type semiconductors, whose conductivity character changes to the metallic one at high temperatures due to the evolution of oxygen from their crystal structure into environment. It was established that partial substitution of barium by strontium in  $\text{NdBaFeCo}_{0.5}\text{Cu}_{0.5}\text{O}_{5+\delta}$  results in the increasing of electrical conductivity, reducing of energy activation of electrical conductivity, thermopower and thermal stability of solid solutions forming at this substitution  $\text{NdBa}_{1-x}\text{Sr}_x\text{FeCo}_{0.5}\text{Cu}_{0.5}\text{O}_{5+\delta}$ .

### References

1. Klyndyuk AI. Perovskite-like Oxides o112 Type: Srtucture, Properties and Possible Applications. Advances in Chemistry Research. V. 5. Ed. by J.C. Taylor. Nova Sci Publ: New-York; 2010. P. 59-105.
2. Lyagaeva J, Danilov N, Tarutin A, Vdovin G, Medvedev D, Demin A, Tsiakaras P. Designing a protonic ceramic fuel cell with novel electrochemically active oxygen electrodes based

**Table 3** Values of TEC ( $\alpha$ ) and apparent activation energy of electrical transport ( $E_o$ ,  $E_S$ ,  $E_m$ ) for the sintered  $\text{NdBa}_{1-x}\text{Sr}_x\text{FeCo}_{0.5}\text{Cu}_{0.5}\text{O}_{5+\delta}$  ceramics

x	$10^6 \cdot \alpha$		$E_o$ , eV (350-700 K)	$E_S$ , eV (400-650 K)	$E_m$ , eV
	$\alpha_{LT}$ , $\text{K}^{-1}$	$\alpha_{HT}$ , $\text{K}^{-1}$			
0.02	15.8	19.3	0.190	0.047	0.143
0.05	16.3	20.0	0.203	0.044	0.159
0.10	16.6	19.1	0.200	0.054	0.146
0.20	16.4	20.4	0.167	0.038	0.129

- on doped  $\text{Nd}_{0.5}\text{Ba}_{0.5}\text{FeO}_{3-\delta}$ . Dalton Trans. 2018;47(24):8149–8157. doi:[10.1039/c8dt01511b](https://doi.org/10.1039/c8dt01511b)
3. Tsvetkov DS, Ivanov IL, Malyshev DA, Sednev AL, Sereda VV, Zuev AY. Double perovskites  $\text{REBaCo}_{2-x}\text{M}_x\text{O}_{6-\delta}$  (RE = La, Pr, Nd, Eu, Gd, Y; M = Fe, Mn) as energy-related materials: an overview. Pure Appl Chem. 2019;19(6):923–940. doi:[10.1515/pac-2018-1103](https://doi.org/10.1515/pac-2018-1103)
  4. Afroze S, Karim AK, Cheok Q, Eriksson S, Azad AK. Latest development of double perovskite electrode materials for solid oxide fuel cell: a review. Front Energy. 2019;13:770–897. doi:[10.1007/s1708-019-0651-x](https://doi.org/10.1007/s1708-019-0651-x)
  5. Kaur P, Singh C. Review of perovskite-structure related cathode materials for solid oxide fuel cell. Ceramics International. 2020;46(5):5521–5535. doi:[10.1016/j.ceramint.2019.11.066](https://doi.org/10.1016/j.ceramint.2019.11.066)
  6. Istomin SYa, Lyskov NV, Mazo GN, Antipov EV. Electrode materials based on complex *d*-metal oxides for symmetrical solid oxide fuel cell. Russ Chem Rev. 2021;90(6):644–676. doi:[10.1070/RCR4979](https://doi.org/10.1070/RCR4979)
  7. Kim J-H, Manthiram A. Layered  $\text{LnBaCo}_2\text{O}_{5+\delta}$  oxides as cathodes for intermediate-temperature solid oxide fuel cell. J Electrochem Soc. 2008;155:3385. doi:[10.1149/1.2839028](https://doi.org/10.1149/1.2839028)
  8. Kim J-H, Manthiram A. Layered  $\text{LnBaCo}_2\text{O}_{5+\delta}$  perovskite cathodes for solid oxide fuel cells: an overview and perspective. J Mater Chem. 2015;3:24195–24210. doi:[10.1039/C5TA06212A](https://doi.org/10.1039/C5TA06212A)
  9. Lin Y, Jin F, Yang X, Nik B, Li Y, He T.  $\text{YBaCo}_2\text{O}_{5+\delta}$ -based double perovskite cathodes for intermediate-temperature solid oxide fuel cells with simultaneously improved structural stability and thermal expansion properties. Electrochim Acta. 2019;297:344–454. doi:[10.1016/j.electacta.2018.11.214](https://doi.org/10.1016/j.electacta.2018.11.214)
  10. Kharton V, Marques F, Atkinson A. Transport properties of solid oxide electrolyte ceramics: a brief review. Solid State Ionics. 2004;174:135–149. doi:[10.1016/j.ssi.2004.06.015](https://doi.org/10.1016/j.ssi.2004.06.015)
  11. Xue J, Shen Y, He T. Performance of double-perovskite  $\text{YBa}_{0.5}\text{Sr}_{0.5}\text{Co}_2\text{O}_{5+\delta}$  as cathode material for intermediate-temperature solid oxide fuel cells. Int J Hydrog Energy. 2011;36:6894–6898. doi:[10.1016/j.ijhydene.2011.02.090](https://doi.org/10.1016/j.ijhydene.2011.02.090)
  12. Cherepanov VA, Aksenova TV, Gavrilova LY, Mikhaleva KN. Structure, nonstoichiometry and thermal expansion of  $\text{NdBa}(\text{Co},\text{Fe})_2\text{O}_{5+\delta}$  layered perovskites. Solid State Ionics. 2011;188:53–87. doi:[10.1016/j.ssi.2010.10.021](https://doi.org/10.1016/j.ssi.2010.10.021)
  13. Zhang S-L, Chen K, Zhang A-P, Li C-X, Li C-Y. Effect of Fe doping on the performance of suspension plasma-sprayed  $\text{PrBa}_{0.5}\text{Sr}_{0.5}\text{Co}_{2-x}\text{Fe}_x\text{O}_{5+\delta}$  cathodes for intermediate-temperature solid oxide fuel cells. Ceramics International. 2017;43:11648–11655. doi:[10.1016/j.ceramint.2017.05.438](https://doi.org/10.1016/j.ceramint.2017.05.438)
  14. Jin F, Li Y, Wang Y, Chu X, Xu M, Zhai Y, Zhang Y, Fang W, Zou P, He T. Evaluation of Fe and Mn co-doped layered perovskite  $\text{PrBaCo}_{2/3}\text{Fe}_{2/3}\text{Mn}_{1/2}\text{O}_{5+\delta}$  as a novel cathode for intermediate-temperature solid oxide fuel cells. Ceramics International. 2018;44:22489–22496. doi:[10.1016/j.ceramint.2018.09.018](https://doi.org/10.1016/j.ceramint.2018.09.018)
  15. Cordaro G, Donazzi A, Pelosato R, Mastropasqua L, Cristiani C, Sora IN, Dotelli G. Structural and Electrochemical Characterization of  $\text{NdBa}_{1-x}\text{Co}_{2-y}\text{Fe}_y\text{O}_{5+\delta}$  as Cathode for Intermediate Temperature Solid Oxide Fuel Cells. J Electrochem Soc. 2020;167:024502. doi:[10.1149/1945-7111/ab628b](https://doi.org/10.1149/1945-7111/ab628b)
  16. Klyndyuk AI, Mosialek M, Kharitonov DS, Chizhova EA, Zimovska M, Socha RP, Komenda A. Structural and electrochemical characterization of  $\text{YBa}(\text{Fe},\text{Co},\text{Cu})_2\text{O}_{5+\delta}$  layered perovskites as cathode materials for solid oxide fuel cells. Int J Hydrog Energy. 2021;46(32):16977–16988. doi:[10.1016/j.ijhydene.2021.01.141](https://doi.org/10.1016/j.ijhydene.2021.01.141)
  17. Yao C., Yang J., Zhang H., Chen S., Lang X, Meng J, Cai K. Evaluation of A-site Ba-deficient  $\text{PrBa}_{0.5-x}\text{Sr}_{0.5}\text{Co}_2\text{O}_{5+\delta}$  ( $x = 0, 0.04, \text{ and } 0.08$ ) as cathode materials for solid oxide fuel cells. J Alloys Compd. 2021;883:160759. doi:[10.1016/j.jallcom.2021.160759](https://doi.org/10.1016/j.jallcom.2021.160759)
  18. Yang Q, Tian D, Liu R, Wu H, Chan Y, Ding Y, Lu X, Lin B. Exploiting rare-earth-abundant layered perovskite cathodes of  $\text{LnBa}_{0.5}\text{Sr}_{0.5}\text{Co}_{1.5}\text{Fe}_{0.5}\text{O}_{5+\delta}$  (Ln = La and Nd) for SOFC. Int J Hydrog Energy. 2021;46(7):5630–5642. doi:[10.1016/j.ijhydene.2020.11.031](https://doi.org/10.1016/j.ijhydene.2020.11.031)
  19. Klyndyuk AI, Chizhova EA. Crystal structure, Thermal Expansion, and Electrical Properties of Layered  $\text{LaBa}(\text{Fe},\text{Co},\text{Cu})_2\text{O}_{5+\delta}$  (Ln = Nd, Sm, Gd) Oxides. Glass Phys Chem. 2014;40(1):124–128. doi:[10.1134/S10876595961401012X](https://doi.org/10.1134/S10876595961401012X)
  20. Klyndyuk AI, Chizhova EA. Structure, Thermal Expansion, and Electrical Properties of  $\text{BiFeO}_3$ - $\text{NdMnO}_3$  Solid Solutions. Inorg Mater. 2015;51(3):272–277. doi:[10.1134/S0020168515020090](https://doi.org/10.1134/S0020168515020090)
  21. Klyndyuk AI, Chizhova EA, Poznyak AI. Preparation and Characterization of  $\text{Bi}_{4-x}\text{Pr}_x\text{Ti}_3\text{O}_{10}$  Solid Solutions. Chimica Techno Acta. 2017;4(4):211–217. doi:[10.15826/chimtech/2017.4.4.01](https://doi.org/10.15826/chimtech/2017.4.4.01)
  22. Shannon RD. Revised effective ionic radii and systematic studies of interatomic distances in halides and chalcogenides. Acta Cryst. 1976;32:751–767. doi:[10.1107/S0567739476001551](https://doi.org/10.1107/S0567739476001551)
  23. Atanassova YK, Popov VN, Bogachev GG, Iliev MN, Mitros C, Psycharis V, Pissas M. Raman- and infrared active phonons in  $\text{YBaCuFeO}_5$ : experimental and lattice dynamics. Phys Rev B. 1993;47:15201–15207. doi:[10.1103/PhysRevB.47.15201](https://doi.org/10.1103/PhysRevB.47.15201)
  24. Klyndyuk AI, Chizhova EA. Physicochemical Properties of  $\text{La}(\text{Ba},\text{M})\text{CuFeO}_{5+\delta}$  (M = Sr, Ca, Mg) solid solutions. Inorg Mater. 2006;42(4):436–442. doi:[10.1134/S0020168506040182](https://doi.org/10.1134/S0020168506040182)
  25. Mott NF, Davis EA. Electronic Processes in Non-Crystalline Materials. 2<sup>nd</sup> ed. New York, USA: Oxford University Press. 1979. 605 p.

# Overview of sorption analysis capabilities for meso- and microporous zeolites nanomaterials

S. Tokmeilova\* , E.V. Maraeva

Saint Petersburg Electrotechnical University «LETI»,  
Prof. Popova St., 5, Saint Petersburg 197376, Russia

\* Corresponding author: [ak\\_saya@mail.ru](mailto:ak_saya@mail.ru)



This article belongs to the regular issue.

© 2021, The Authors. This article is published in open access form under the terms and conditions of the Creative Commons Attribution (CC BY) license (<http://creativecommons.org/licenses/by/4.0/>).

## Abstract

In this paper we consider the main application features of the thermal desorption method of inert gases, implemented on the Sorbi MS (Meta, Russia) device, for the analysis of meso- and microporous materials. Recommendations on the choice of measurement modes for stable operation of the Sorbi MS device are offered (including recommendations on mass, sample preparation mode). The article presents the results of the micropores analysis by the t-plot and Sing method.

## Keywords

micropores  
mesopores  
capillary condensation  
sorption hysteresis

Received: 27.04.2021

Revised: 12.06.2021

Accepted: 30.06.2021

Available online: 07.07.2021

## 1. Introduction

Gas sorption methods are commonly used to characterize porous materials. Porous materials are widely used in micro- and nanoelectronics. According to the classification of pores by size, micropores are less than 2 nm in size, mesopores are in the range from 2 to 50 nm [1]. At present, nitrogen sorption at 77 K has become a standard tool for the analysis of materials with pores in a range of 0.5–50 nm. The mechanism of nitrogen sorption at 77 K occurs in the following way. At a low relative pressure (0.02–0.1), the filling of micropores with adsorbate begins. The monolayer adsorption occurs after the completion of adsorption in micropores. Capillary condensation is observed in relatively small mesopores when the relative pressure and pore width correspond to the Kelvin equation. The desorption isotherm is obtained by reversing the adsorption process, releasing the liquid adsorbate and decreasing the equilibrium relative pressure [2]. The evaporation process takes place from the meniscus of the condensed liquid.

In the case of polymolecular adsorption, the adsorption potential interaction does not change with the distance from the surface of micropores, as a result of dispersion potentials overlapping of closely spaced pore walls [3]. As a result, adsorption in the entire volume of micropores becomes equiprobable to adsorption on their surface (micropores volumetric filling). The adsorption potential interaction of adsorptive molecules with microporous materials is much higher than with the surface of mesoscale

materials. All this together determines some peculiarities and imposes certain restrictions on the applicability of the Brunauer-Emmett-Teller (BET) method. Therefore, other procedures are used for the micropore adsorption isotherms analysis, the so-called comparative methods of analysis, which make it possible to isolate the contribution of adsorption in the volume of micropores and to calculate the size of the mesopores and macropores surface. Currently, a large number of comparative methods are known that are used to determine the specific surface area of a microporous material and to estimate the volume of micropores in the presence of mesopores: t-method, Sing's  $\alpha$ s-method and others.

The works [4–7] illustrating the current state of the question of the specific surface area analysis of mesoporous materials are presented. Mesoporous materials are widely used in practice (bioengineering, sensorics of gaseous media and environmental monitoring, power engineering, lithium-ion batteries), are used as adsorbents and catalysts for oil refining processes. In all cases, the porous structure parameters play a key role.

The paper [4] presents and discusses the kinetic results of nitrogen adsorption and desorption experiments performed at 77 K on one aluminum-based and three materials based on carbon, differing in their microporous and mesoporous nature. The paper is devoted to the study of transport phenomena during adsorption / desorption experiments in pores of various sizes. The authors of the article noted that the rates of transport phenomena

change significantly with the gradual filling / emptying of the pores.

The authors of [5] synthesized and investigated CoO-3D ordered mesoporous carbon nitride (CoO@mpgCN) catalyst. The authors managed to find out that the significant catalytic performance of CoO@mpgCN was due to its uniformly distributed mesopores, large specific surface area, and high electron transferability at the active CoO sites. The textural parameter and the mesoporous extent of materials originated from parent template were examined by nitrogen adsorption-desorption isotherm along with corresponding BET surface area and pore distribution analyses.

The authors of [6] aimed to explore a facile route to synthesize mesoporous zinc silicate composites. The specific surface area and the pore properties of the samples were tested by the Brunauer-Emmett-Teller (BET) method based on N<sub>2</sub> adsorption / desorption measurements on Quantachrome Autosorb-IQ2. The authors provided the N<sub>2</sub> adsorption / desorption isotherms and pore size distributions of ZS-3 and ZS-5 that are rather different in structure. The fact that the structure is mesoporous is indicated by the increase of adsorbed nitrogen at relative pressure  $P > 0.45$  and related to the multilayer adsorption and capillary condensation of N<sub>2</sub>. The excellent adsorption property endows the composite with potential application in the field of dye wastewater treatment.

The authors of [7] attempted to enhance nitrogen adsorption capacity modified X zeolite adsorbent. For this, procedures including both NH<sub>4</sub><sup>+</sup> treatment and Ca<sup>2+</sup> ion-exchange were carried out. These modifications lead to a hierarchical mesopore-micropore structure with a multilayer N<sub>2</sub> adsorption capacity. The properties of adsorbents are characterized by N<sub>2</sub> adsorption-desorption in 77 K, XRD, and XRF analysis. In paper [7] adsorption isotherms are modeled by Langmuir, Dual-Site Langmuir (DSL), Freundlich, and Langmuir-Freundlich (Sips) models, and the corresponding parameters are determined. These adsorbents can be used effectively in the helium purification by the pressure swing adsorption (PSA) process, which is based on nitrogen adsorption.

It is known that the zeolites considered in this work are microporous materials. However, catalytic processes require materials containing both meso- and macropores. At the same time, the advanced system of zeolite micropores has a significant effect on the rate of the reactions. In this regard, it is necessary to develop analysis techniques that provide simultaneous control of the micro- and mesoporous structure of materials.

The aim of this paper is to consider the application peculiarities of the thermal desorption method of inert gases, implemented on the Sorbi MS (Meta, Russia) device, for the analysis of meso- and microporous zeolite materials.

## 2. Experimental

In this work, zeolites of the type ZSM-5 (samples 1,3) and BETA (samples 2,4-6) were investigated. Aluminum hydroxide (AH), including silica addition, was selected as the binder. The sample synthesis features and the selection of the peptizers are shown in Table 5.

Zeolites were synthesized at the Irkutsk National Research Technical University. In the previous paper [8], the results of the studying the properties of compositions in the mesopore range are presented; here we will emphasize the analysis of micropores.

Adsorption isotherms were built on the basis of the sorption study data obtained. The samples were studied by nitrogen sorption at 77 K on the Sorbi MS device. The device works by comparing the volumes of adsorbate gas sorbed by the test sample and the standard sample. The specific surface area is measured using the 4-point BET method. Micropores volume was determined on the basis of analysis of inert gas adsorption isotherms.

## 3. Results and Discussion

### 3.1. Investigation of capillary condensation processes, sorption hysteresis

A characteristic feature of adsorption in mesopores is associated with capillary condensation, which leads to filling the mesopores volume with a liquid adsorbate phase at a relative pressure, for example, nitrogen vapor at 77 K,  $0.4 < P/P_0 < 1$ . As a rule, the process of capillary condensation is irreversible. This means that the magnitude of sorption with increasing pressure of the sorbent does not coincide with the magnitude of sorption with decreasing pressure. In this case, a characteristic hysteresis is formed on the sorption isotherm, formed by mismatched branches of adsorption and desorption (Fig. 1) [3].

### 3.2. Recommendations on the choice of measurement modes of the Sorbi MS device

During researching the parameters of the nanomaterials porous structure by the sorption method, it is important to correctly estimate the mass of the adsorbent material required for the study, select the sample preparation mode, and set the range of the relative partial pressure variation of the adsorbate gas at which the measurement will be carried out.

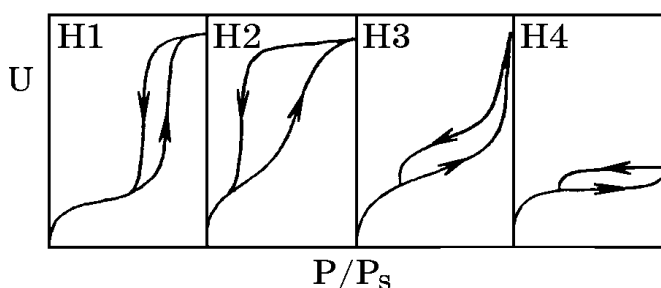


Fig. 1 Characteristic types of capillary-condensation hysteresis loops according to the IUPAC classification. Adapted from [3]

### 3.2.1. Determination of the analyzed material mass and sample preparation

The features of the thermal desorption method realized in Sorbi MS are discussed in [9,10]. When studying compositions by the thermal desorption method of nitrogen, the choice of the analysed material mass is determined by two factors: the possibility of obtaining a stable desorption signal, which is used to calculate the volume of desorbed gas, and the range of the total measured surface  $S = S_{sp} \cdot m$ . For example, the selected masses for various series of zeolite compositions that provide a stable desorption signal are shown in Table 1.

### 3.2.2. Modes selection and sample preparation of the analyzed material

Sample preparation of the analysed material, as a rule, consists in controlled heating of the sample in a flow of inert gas (helium). Preparation is necessary, first of all, to remove moisture and surface contamination. Variable sample preparation modes are heating temperature and time. Table 2 shows, for example, the results of measuring the parameters of the porous structure of some samples depending on the conditions of preliminary degassing.

Also all samples were subjected to a single annealing procedure in a muffle furnace for 1 hour. This procedure is required in case of long-term storage or transportation of samples in high humidity conditions. The results of measuring the specific surface area for a sample of the BEA type are presented in Table 3.

As can be seen from Table 3, in the case of long-term storage of zeolite samples in high humidity conditions, the measured specific surface area of the samples decreases by 2–3 times. Zeolites annealing at a temperature of 500 °C restores the specific surface area by removing moisture from the micro- and mesoporous system. In the study of zeolites, such heat treatment is similar to the annealing at the final stage of their preparation does not lead to structure destruction and is recommended.

### 3.2.3. Measurement in the given range of the relative partial pressures of the adsorbate gas $P/P_0$

The range selection of  $P/P_0$  values is determined by the investigated porous structure parameter. The measurement of the specific surface area by the BET method, the external surface and the construction of the size distribution of mesopores suggest the choice of different study modes.

For example, the  $P/P_0$  parameters that are selected on the Sorbi MS device used in this work are listed in Table 4.

### 3.3. The micropores volume determination of a series of zeolite compositions by the Sing and t-plot methods

For the successful and high-quality application of porous materials, the control of their parameters and properties is an important criterion. Analysis of microporous structure parameters in zeolite compositions was carried out in

**Table 1** Selected masses for various series of zeolite compositions

Series	BEA+2MNaOH		BEA	
Mass, mg	83	150	49	211
$S_{sp}$ value at standard conditions of sample preparation, $m^2/g$	296.6	Exceeding the maximum measurable desorption signal	303.4	Exceeding the maximum measurable desorption signal

**Table 2** Specific area values for different sample preparation modes

	$T$ Prep, °C	$t$ Prep, min	$S_{sp}$ , $m^2/g$
	-	-	99.79
BEA+2MNaOH	150	20	296.6
	150	45	399.2
	300	15	434.4

**Table 3** Specific area values for different sample preparation modes before and after annealing at 500 °C

	$T$ Prep, °C	$t$ Prep, min	$S_{sp}$ , $m^2/g$
BEA before annealing	-	-	170
	150	60	366.1
BEA after annealing	-	-	453
BEA after annealing, 3 days later	-	-	300
	150	60	470

**Table 4** The value range of  $P/P_0$

Investigated parameter	Method	Range of relative partial pressures of adsorbate gas $P/P_0$
Specific surface area	BET	6% to 20%
Micropore indication	t-plot method	15% to 40%
External surface of mesopores, size distribution of mesopores	Capillary condensation of an inert gas	6% to 97%

this paper. Zeolites of the type ZSM-5 (samples 1,3 in Table 5) and BETA (samples 2,4–6 in Table 5) were used.

Studies of the zeolites porous structure were carried out by low-temperature nitrogen adsorption on a Sorbi MS device (t-plot method).

As an alternative method for estimating the micropores volume, a comparative Sing method is proposed. It is based on the use of the relative adsorption value  $\alpha_s$  on the reference sample.

The value  $\alpha_s$  is calculated from the ratio of the current adsorption value  $V$  to adsorption at the relative pressure  $P/P_0 = 0.4$ . The reference is a non-porous zeolite (without heating) of the same chemical nature as the sample under study. Using normalized value we rebuild previously constructed adsorption isotherms into dependence of type  $V = f(V/V_{0.4})$ , replacing relative pressure by value  $\alpha_s$ . The segment, cut off on the ordinate axis, is the value by which the micropores volume is then calculated.

The obtained t-plot and Sing micropore volume values are shown in Table 5.

**Table 5** Micropore volume values by the t-plot and Sing method

Sample №	Sample composition zeolite/AH, wt%	AH producer	Peptizer	Micropores volume (t-plot method), cm <sup>3</sup> /g	Micropores volume (Sing method), cm <sup>3</sup> /g
1	ZSM-5	-	-	0.07	0.07
2	BEA	-	-	0.066	0.09
3	70 ZSM -5/30 AH	Sasol	aqueous solution of nitric acid	0.053	0.065
4	70 BEA /30 AH-1	Sasol	aqueous solution of nitric acid	0.039	0.074
5	70 BEA /30 AH-2	OAO AZK and OS	aqueous solution of nitric acid	0.1	0.1
6	70 BEA /30 AH-3	OAO AZK and OS	mixture of aqueous solutions of nitric acid and ammonia (1:1)	0.072	0.097

As it can be seen, the micropore volume values calculated by Sing do not differ significantly compared to the values taken from the Sorbi MS device. Thus, it is possible to estimate the volume of micropores by both the t-plot method and the comparative Sing method. The analysis showed that the largest micropores volume (0.1 ml/g) is typical for samples of series 5, where in the synthesis process an aqueous solution of nitric acid was used as a peptizer, and aluminum hydroxide from the manufacturer OAO AZK and OS was used as a binder. Replacement of the peptizer (sample 6 in Table 5) led to a slight decrease in the micropores volume in the composition. However, such a replacement results in an increase in the total specific surface area [8] and the total pore volume.

#### 4. Conclusions

The paper considers the method application features of nitrogen thermal desorption for the study of microporous materials on the example of zeolite composition.

The recommended mass values for obtaining a stable desorption signal and the recommended modes of sample preparation of zeolite compositions were selected. As a rule, in the study of materials by the thermal desorption method of inert gases, an insufficient mass of the sample can act as a significant limitation for the analysis. In the case of studying zeolite compositions, on the contrary, too large an adsorbent mass can lead to an incorrect sensor signal for thermal conductivity and peak truncation.

Nitrogen adsorption at 77 K on a series of zeolite compositions was investigated. It was shown that using analysis sorption methods, it is possible to estimate the volume micropores by the t-plot and Sing method.

#### References

- Everett D. Manual of Symbols and Terminology for Physicochemical Quantities and Units, Appendix II: Definitions, Terminology and Symbols in Colloid and Surface Chemistry. Pure and Applied Chemistry. 1972;31(4):577-638. doi:[10.1351/pac197231040577](https://doi.org/10.1351/pac197231040577)
- Wang G, Wang K, Ren T. Improved analytic methods for coal surface area and pore size distribution determination using 77K nitrogen adsorption experiment. Int J Min Sci Technol. 2014;24(3):329-334. doi:[10.1016/j.ijmst.2014.03.007](https://doi.org/10.1016/j.ijmst.2014.03.007)
- Gavrilov VY. Fiziko-himicheskie osnovy adsorbciionnogo analiza dispersnyh i poristyh materialov [Physicochemical bases of adsorption analysis of dispersed and porous materials]. Novosibirsk: NCTC; 2007. 67 p. Russian.
- Zelenka T. Adsorption and desorption of nitrogen at 77 K on micro- and mesoporous materials: Study of transport kinetics. Journal of Microporous and Mesoporous Materials. 2016;227:202-209. doi:[10.1016/j.micromeso.2016.03.009](https://doi.org/10.1016/j.micromeso.2016.03.009)
- Nguyen TB, Huang CP, Doong RA, Chen CW, Dong CD. CoO-3D ordered mesoporous carbon nitride (CoO@mpgCN) composite as peroxymonosulfate activator for the degradation of sulfamethoxazole in water. Journal of Hazardous Materials. 2021;401:123320. doi:[10.1016/j.jhazmat.2020.123326](https://doi.org/10.1016/j.jhazmat.2020.123326)
- Dong GY, Tian GY, Gong LL, Tang QG. Mesoporous zinc silicate composites derived from iron ore tailings for highly efficient dye removal: Structure and morphology evolution. Journal of Microporous and Mesoporous Materials. 2020;305:110352. doi:[10.1016/j.micromeso.2020.110352](https://doi.org/10.1016/j.micromeso.2020.110352)
- Hadis M, Jafar T, Babak M. Enhanced nitrogen adsorption capacity on Ca<sup>2+</sup> ion-exchanged hierarchical X zeolite. Separation and Purification Technology. 2021;264:118442. doi:[10.1016/j.seppur.2021.118442](https://doi.org/10.1016/j.seppur.2021.118442)
- Kononova IE, Maraeva EV, Skornikova SA, Moshnikov VA. Influence of binder on porous structure of zeolite compositions and their catalytic activity. Glass Physics and Chemistry. 2020;46(2):162-169. doi:[10.1134/S1087659620020066](https://doi.org/10.1134/S1087659620020066)
- Gracheva IE, Moshnikov VA, Maraeva EV, Karpova SS, Aleksandrova OA, Alekseyev NI, Kuznetsov VV, Olchowick G, Semenov KN, Startseva AV, Sitnikov AV, Olchowick JM. Nanostructured materials obtained under conditions of hierarchical self-assembly and modified by derivative forms of fullerenes. Journal of non-crystalline solids. 2012;358(2):433-439. doi:[10.1016/j.jnoncrsol.2011.10.020](https://doi.org/10.1016/j.jnoncrsol.2011.10.020)
- Maraeva EV, Permiakov NV, Kedruk YY, Gritsenko LV, Abdullin KhA. Creating a virtual device for processing the results of sorption measurements in the study of zinc oxide nanorods. Chimica Techno Acta. 2020;7(4):154-158. doi:[10.15826/chimtech.2020.7.4.03](https://doi.org/10.15826/chimtech.2020.7.4.03)

# Sensitivity of the phenoxy derivatives of 2,4-dihydro-5*H*-[1,2,3]triazolo[4,5-*d*]pyrimidin-5-ones to acidic and basic stimuli

Alexander K. Eltyshev , Nataliya P. Belskaya\* 

Ural Federal University, 19 Mira St., Yekaterinburg 620002, Russia

\* Corresponding author: [n.p.belskaya@urfu.ru](mailto:n.p.belskaya@urfu.ru)

This article belongs to the regular issue.

© 2021, The Authors. This article is published in open access form under the terms and conditions of the Creative Commons Attribution (CC BY) license (<http://creativecommons.org/licenses/by/4.0/>).



## Abstract

Herein we report the research on the sensitivity of six hydroxy derivatives of dihydrotriazolopyrimidines (HO-DTP) to acids and bases. The UV/Vis and fluorescence spectra of these compounds were investigated with the addition of the acids and bases. Spectral data revealed the strong red shifts for emission and absorption maxima in the presence of KOH and NaOH. Moreover, two DTPs demonstrated strengthening of the emission intensity. The obtained results and data published in our previous paper demonstrated the strong and selective sensory response of DTPs to the acids and bases and elucidated relationships between the structure and sensitivity to the environment. This finding allowed us to manage these properties by introducing the combination of substituents and functionalities into the heterocyclic core. Thus, investigations demonstrated the potential of the application of DTPs as chemo- and fluorosensors for selective detection of acids and bases.

## Keywords

dihydrotriazolopyrimidines  
acids  
bases  
fluorescence response  
chemosensor

Received: 27.07.2021

Revised: 11.08.2021

Accepted: 16.08.2021

Available online: 17.08.2021

## 1. Introduction

Fluorophores sensitive to external stimuli are attractive compounds owing to their application in contaminant analysis environment, electrochemical sensors, biosensing, and detection of toxins [1]. Extensive studies have been directed for development of new fluorescent sensory organic materials which are able to respond on the external stimuli via changes of their absorption or fluorescence characteristics. These stimuli may include temperature, scattered light, pH, and even nature of solvent [2].

Monitoring the pH levels in high alkaline media is of wide importance for many industrial processes, in gas scrubbers, wastewater monitoring, treatment of the plants and concrete structures [3, 4]. The sensing materials suitable for measurement of high alkali media are very limited. In recent years, a few fluorescent sensors in an alkaline pH region have been reported [5-7].

Recently we reported the synthesis and photophysical properties of new blue and blue-green fluorophores derived on dihydro-1,2,3-triazolopyrimidine core (DTP) [8]. These fluorophores exhibited multifunctional properties and showed good fluorescence in solutions (with QY up to 88%, Stokes shift (SS) ~151 nm and  $\lambda_{em}$  up to 534 nm). We

suggested and developed synthetic procedure providing various DTPs with different electronic structures (A- $\pi$ -D and D- $\pi$ -A). These compounds showed selective reversible acidochromism in solution and in a solid state in the presence of HCl vapor.  $^1\text{H}$  NMR investigation showed that the pyrimidine and *N-tert*-cycloalkylamine moieties are the binding sites responsible for specific sensory response to the acids.

Current research is focused on the investigation of the photophysical characteristics of the phenoxyderivatives of triazolopyrimidines (OH-DTPs) bearing OH-functionality in the different positions of the molecule and studies of their response to the different acids and bases as external stimuli.

Hydroxy group is very attractive from a biological point of view. Numerous biocompounds include OH-functionalities in their structure (alkaloids, flavonoids, isoflavonoids, terpenoids, lipids, fatty acids, amino acids etc.) [9, 10]. Bioluminescent molecule (luciferin) and different synthetic fluorophores bearing this substituent are well known [11-19]. Introduction of hydroxy groups usually causes the changes in electronic properties owing to its strong electron-donating nature and increases the intramolecular charge transfer (ICT) effect. Moreover, hydroxy

group can strengthen the fluorophore participation in intra- and intermolecular noncovalent bonding to enhance the molecule rigidity and take part in self-organization. Finally, hydroxy groups [20] can be transformed into the salts, which are more soluble in water. Deprotonation of hydroxy group may influence the optical properties of the resulted salts.

## 2. Experimental

UV-Vis absorption spectra were recorded on a Perkin-Elmer Lambda 35 UV-Vis spectrophotometer (Shelton, CT USA). Fluorescence of the sample solutions was measured using a Hitachi F-7000 spectrophotometer (Tokyo, Japan). The excitation wavelength was at the absorption maxima. Atmospheric oxygen contained in solutions was not removed. Concentration of the compounds in the solution was  $5.0 \cdot 10^{-5}$  M and  $5.0 \cdot 10^{-6}$  M for absorption and fluorescence measurements, respectively. The relative fluorescence quantum yields (QY) were determined using quinine sulfate in 0.1 M  $H_2SO_4$  as a standard (QY = 0.546). Absolute quantum yield study was performed on Horiba FluoroMax 4 Spectrofluorometer (Kyoto, Japan) with Quanta- $\phi$  integrating sphere using FluorEssence 3.5 Software.

DTPs **1a-e**, **2a-c** and **3a-b** were prepared according to procedures reported in the literature and their spectral characteristics were identical to the published data [8, 21].

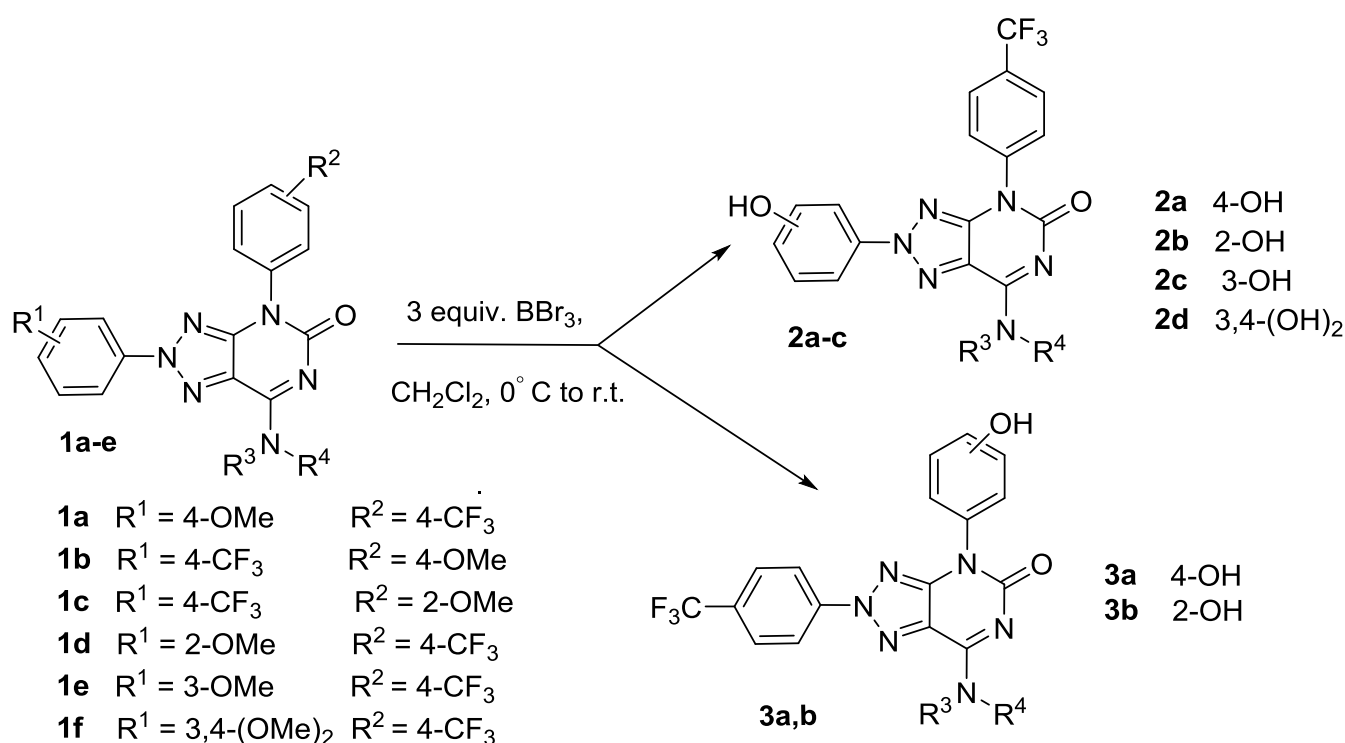
## 3. Results and Discussion

2-(Hydroxyphenyl)-4-(4-trifluoromethylphenyl)-2,4,5-*H*-[1,2,3]triazolo[4,5-*c*]pyrimidines (HO-DTPs) **2a-c** and **3a-b**

were prepared via the demethylation of their methoxycongeners by using  $BBr_3$  solution in dichloromethane with special temperature profile regime (Scheme 1).

The spectral and analytical data of DTPs **2a-d** and **3a, b** were consistent with the published data [21]. Absorption and emission spectra recorded earlier showed insignificant difference in long wavelength maxima positions compared to the corresponding MeO-DTPs derivatives. At the same time HO-DTPs quantum yields (QY) of were in 6-40-fold lower. Only HO-DTP **2a** demonstrated good QY compared to QY of DTP **1a** in DMSO (40.1% and 39.4%, respectively) (Table 1). However, in the other solvents QYs of HO-DTP **2a** decreased significantly.

The preliminary investigation of the influence of the different acids and bases on the optical properties of the HO-DTP solutions in DMSO showed the absence of any effect. Therefore, we included only trifluoroacetic acid (TFA) into further consideration. Absorption and emission spectral data of the HO-DTPs **2a-d** and **3a,b** in the presence of different organic bases, alkalis and TFA are collected in Table 1. Analysis of the Table 1 data showed that addition of the KOH (5% water solution) caused red shift of the absorption and emission maxima by 20-121 and 22-169 nm, respectively, and for the most HO-DTP QYs were decreased. Addition of TFA did not affect the photophysical properties for the most compounds, except the DTP **2b**. In this case, the maxima of absorption and emission bands were redshifted for 30 nm and 11 nm accordingly. Unlike most acids, the addition of KOH solution caused dramatic changes in the photophysical properties of DTPs **2a-d**, **3a,b**. Thus, in fluorescence spectra a strong bathochromic shift of the emission maxima of 57-169 nm was observed



Scheme 1 Synthesis of OH-DTPs **2a-d** and **3a,b**

**Table 1** Absorption and emission data for DTPs **2a-d**, **3a,b** solution ( $c = 5 \cdot 10^{-6}$  M) in DMSO before and after the addition of 500 eq. of TFA or KOH (5% solution in water)

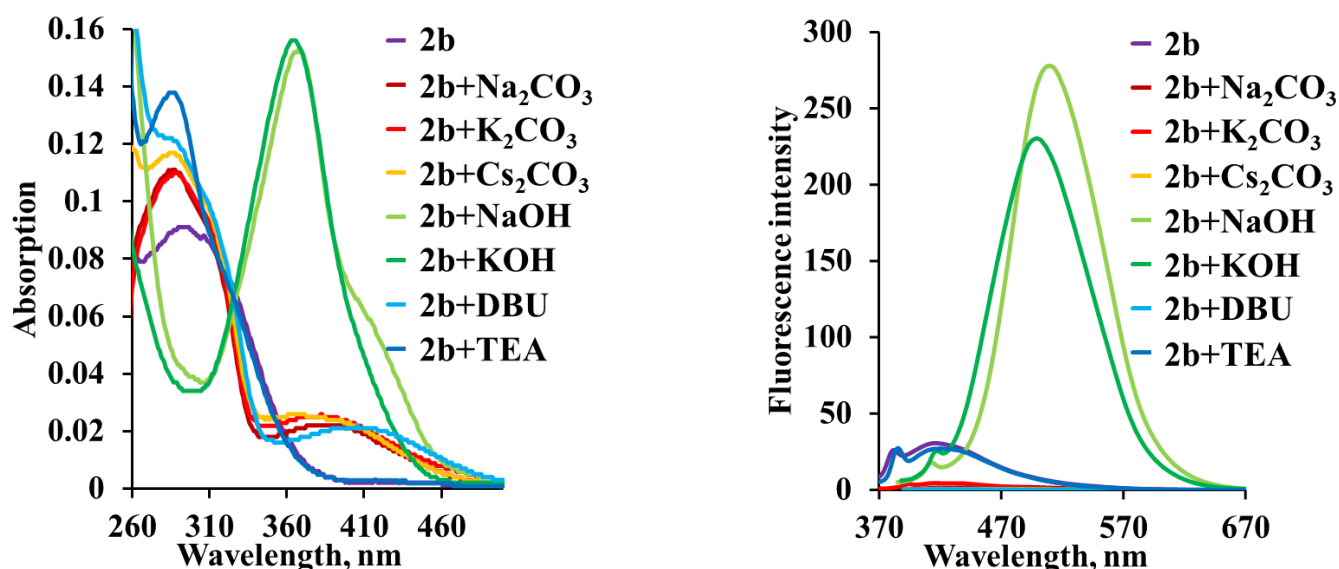
Entry	Compound	Acid/Base	$\lambda_{\text{abs}}$ , nm	$\lambda_{\text{em}}$ , nm	SS, nm/cm <sup>-1</sup>	QY, %
1		-	347	441	94/6143	40.1
2	<b>2a</b>	TFA	347	441	94/6143	18.2
3		KOH	375	498	123/6586	19.8
4		-	296	419	123/9917	0.4
5	<b>2b</b>	TFA	326	408	82/6165	0.6
6		KOH	364	503	139/7592	7.5
7		-	340	416	76/6903	0.5
8	<b>2c</b>	TFA	331	414	83/6057	0.8
9		KOH	360	500	140/7778	5.9
10		-	356	472	116/6903	1.1
11	<b>2d</b>	TFA	360	450	90/5556	0.6
12		KOH	418	530	110/5056	0.6
13		-	347	432	85/5670	0.6
14	<b>3a</b>	TFA	347	420	74/5092	0.6
15		KOH	423	500	77/3641	-
16		-	341	416	75/5287	0.3
17	<b>3b</b>	TFA	339	404	65/4746	0.2
18		KOH	492	585	93/3231	-

along with the QY decrease for the most DTPs, with the exception for **2b** and **2c**. DTPs **2b** and **2c**, bearing hydroxy group at ortho- and meta-position of aromatic ring A showed the large increase of their QYs from 0.4 and 0.5% (in pure DMSO) to 7.5 and 5.9%, respectively. Thus, hydroxyl DTP derivatives display different sensitivity to the alkali media depending on their structure.

These results inspired us to check the influence of the set of bases on the photophysical properties of DTP **2b** (Fig. 1) under the same conditions. These data indicated a significant effect of bases on both the absorption and the emission of DTP **2b**. In all the cases, the absorption and emission maxima were redshifted in range 68-110 nm and 19-62 nm, respectively. The effect of TEA stimulus deviates from common trend and consists in slight blue shifting (4 nm) (Fig. 1). The most effective were alkalis (NaOH and KOH), whose addition to the HO-DTPs **2b** solution in

DMSO led to large redshifts (61-62 nm) and substantial (in 9-10 folds) increasing of emission intensity. Visual emission change from colorless to green was observed for the DTPs **2b** solution after the addition of 50 eq of NaOH solution, which further developed to bright green-yellow emission (Fig. 2).

Further, we studied changes in absorption and emission spectra of HO-DTP **2c** induced by NaOH (Fig. 3). HO-DTP **2c** was almost non-fluorescent in DMSO solution ( $c = 5 \cdot 10^{-6}$  M), while the addition of NaOH caused an appearance of a new fluorescence maximum at 504 nm (Fig. 3b). The intensity of this new maximum was enhanced drastically upon the increasing amounts of NaOH and reached the saturation at 300 eq. Changes in absorption were also registered. In this case new maximum was located at 395 nm when 25 eq. of NaOH solution were added, and further NaOH addition led to increasing of this

**Fig. 1** UV-Vis absorption (left) and emission (right) spectra of DTP **2b** after addition of different bases (for absorption and emission  $c = 5 \cdot 10^{-6}$  M)

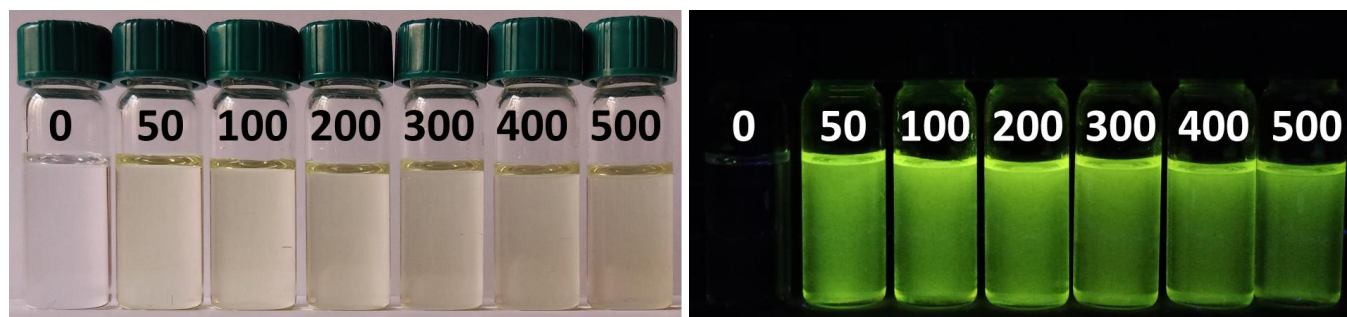


Fig. 2 The titration of HO-DTP **2b** solution in DMSO with the 5% NaOH solution under sunlight (left) and UV-irradiation (right)

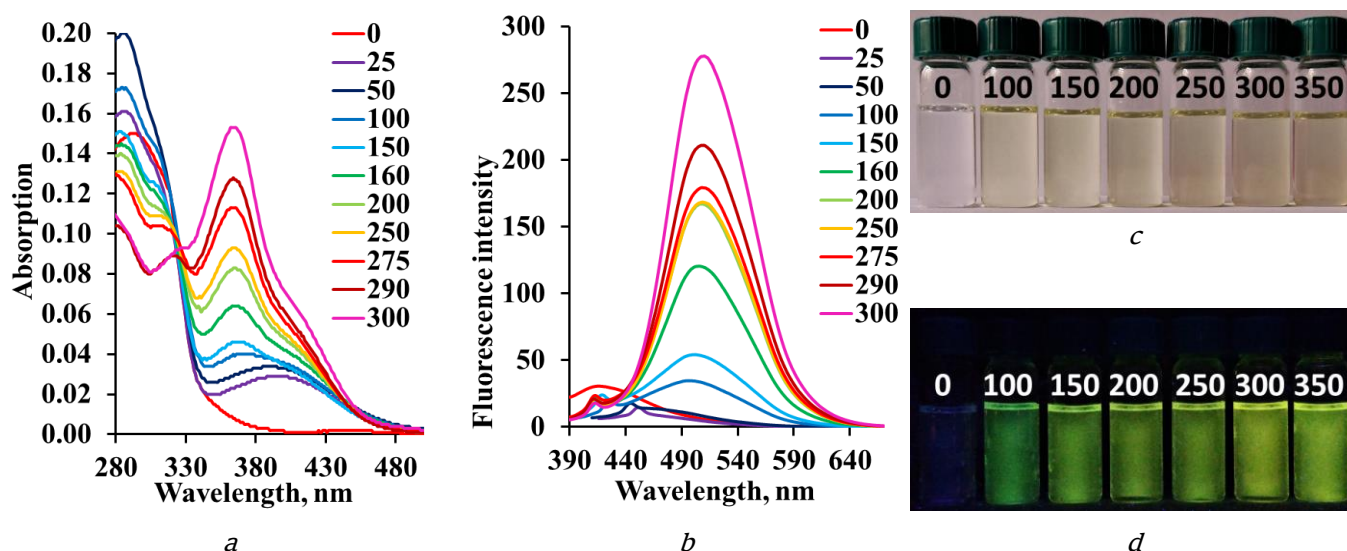


Fig. 3 Absorption (a) and emission (b) of DTP **2c** solution in DMSO with addition of different eq. of NaOH. Photos of the solutions of **2c** in DMSO with increasing amount of NaOH under sunlight (c) and UV-irradiation (d).

maximum intensity and simultaneous appearance of the new maximum at 368 nm. Isosbestic points in absorption spectra emerged at 325 and 425 nm and this suggests a reactive equilibrium between these two components.

#### 4. Conclusions

In conclusion, we reported the results of the investigation of the optical properties of hydroxy substituted DTPs in the presence of different acids or bases. Hydroxy-DTPs demonstrated a pronounced fluorescence response in alkaline environment, which resulted in strong bathochromic shift of the absorption and emission maxima along with enhancement of the intensity of the fluorescence. However, they did not display any noticeable perceptible response to organic or mineral acids. Thus, introducing of the OH group onto the dihydro-1,2,3-triazole structure led to the sharp change in response of these compounds to basic/alkali stimuli. These results together with our recent ones demonstrated that acid/base sensitivity of the DTPs can be adjusted by varying the substituents and functionalities attached to the dihydropyrimidine core.

#### Acknowledgments



The work was carried out with the financial support of the Russian Foundation for Basic Research (Grant 19-33-90184).

#### References

1. Qian J, Zhang Y, Liu X, Xia J. Carbazole and fluorene polyani-line derivatives: Synthesis, properties and application as multiple stimuli-responsive fluorescent chemosensor. *Talanta*. 2019;204:592-601. doi:[10.1016/j.talanta.2019.06.038](https://doi.org/10.1016/j.talanta.2019.06.038)
2. Valeur B, Berberan-Santos MN. *Molecular Fluorescence*. Weinheim: Wiley VCH; 2013. 592 p.
3. Srinivasan R, Phillips TE, Barger CB, Carlson MA, Schemm ER, Saffarian HM. Embedded micro-sensor for monitoring pH in concrete structures. *Proc SPIE*. 2000;3988:40-4. doi:[10.1117/12.383169](https://doi.org/10.1117/12.383169)
4. Basheer PAM, Grattan KTV, Sun T, Long AE, McPolin D, Xie W. Fibre optic chemical sensor systems for monitoring pH changes in concrete. *Proc SPIE*. 2004;5586:144-53. doi:[10.1117/12.601198](https://doi.org/10.1117/12.601198)
5. Hecht M, Kraus W, Rurack K. A highly fluorescent pH sensing membrane for the alkaline pH range incorporating a BODIPY dye. *Analyst*. 2013;138(1):325-32. doi:[10.1039/C2AN35860C](https://doi.org/10.1039/C2AN35860C)

6. Gotor R, Ashokkumar P, Hech M, Keil K, Rurack K. Optical pH sensor covering the range from pH 0-14 compatible with mobile-device readout and based on a set of rationally designed indicator dyes. *Anal Chem.* 2017;89(16):8437-44. doi:[10.1021/acs.analchem.7b01903](https://doi.org/10.1021/acs.analchem.7b01903)
7. Pfeifer D, Klimart I, Borisov SM. Ultra-bright red-emitting photostable perylene bisimide dyes: new indicators for ratiometric sensing of high pH or carbon dioxide. *Chem Eur J.* 2018;24:10711-20. doi:[10.1002/chem.201800867](https://doi.org/10.1002/chem.201800867)
8. Eltyshev AK, Sunstova PO, Karmatskaia KD, Taniya OS, Slepukhin PA, Benassi E, Belskaya NP. An effective and facile synthesis of new blue fluorophores on the basis of an 8-azapurine core. *Org Biomol Chem.* 2018;16(48):9420-29. doi:[10.1039/C8OB02644K](https://doi.org/10.1039/C8OB02644K)
9. Li X, Peng Y, Liu H, Xu Y, Wang X, Zhang C, Ma X. Comparative studies on the interaction of nine flavonoids with trypsin. *Spectrochim Acta A.* 2020;238:118440. doi:[10.1016/j.saa.2020.118440](https://doi.org/10.1016/j.saa.2020.118440)
10. Yao J, He Y, Su N, Bharath SR, Tao Y, Jin JM, Chen W, Song H, Tang SY. Developing a highly efficient hydroxytyrosol whole-cell catalyst by de-bottlenecking rate-limiting steps. *Nat Commun.* 2020;11:1515. doi:[10.1038/s41467-020-14918-5](https://doi.org/10.1038/s41467-020-14918-5)
11. Jadhav AS, Carreira-Blanco C, Fernández B, González Fernández S, Malkhede DD, Mosquera MM, Ríos Rodríguez MC, Rodríguez-Prieto F. Firefly luciferin precursor 2-cyano-6-hydroxybenzothiazole: Fluorescence à la carte controlled by solvent and acidity. *Dyes Pigm.* 2020;177:108285. doi:[10.1016/j.dyepig.2020.108285](https://doi.org/10.1016/j.dyepig.2020.108285)
12. Aysha TS, El-Sedik MS, Mohamed MBI, Gaballah ST, Kamel MM. *Dyes Pigm.* 2019;170:107549. doi:[10.1016/j.dyepig.2019.107549](https://doi.org/10.1016/j.dyepig.2019.107549)
13. Zhang J, Lia J, Chen B, Kan J, Jiang T, Zhang W, Yue J, Zhou J. An off-on fluorescent probe for real-time sensing the fluctuations of intracellular pH values in biological processes. *Dyes Pigm.* 2019;170:107620. doi:[10.1016/j.dyepig.2019.107620](https://doi.org/10.1016/j.dyepig.2019.107620)
14. Bondar K, Bokan M, Gellerman G, Patsenker LD. Water-soluble 4-hydroxystyryl and 4-hydroxyphenylbutadienyls dyes with switchable fluorescence. *Dyes Pigm.* 2020;172:107801. doi:[10.1016/j.dyepig.2019.107801](https://doi.org/10.1016/j.dyepig.2019.107801)
15. Seo MH, Han J, Jin Z, Lee DW, Park HS, Kim HS. Controlled and Oriented Immobilization of Protein by Site-Specific Incorporation of Unnatural Amino Acid. *Anal Chem.* 2011;83(8):2841-45. doi:[10.1021/ac103334b](https://doi.org/10.1021/ac103334b)
16. Eichelbaum K, Winter M, Berriel Diaz M, Herzig S, Krijgsveld J. Selective enrichment of newly synthesized proteins for quantitative secretome analysis. *Nat Biotechnol.* 2012;30:984-90. doi:[10.1038/nbt.2356](https://doi.org/10.1038/nbt.2356)
17. Raliski BK, Howard CA, Young DD. Site-Specific Protein Immobilization Using Unnatural Amino Acids. *Bioconjugate Chem.* 2014;25:1916-20. doi:[10.1021/bc500443h](https://doi.org/10.1021/bc500443h)
18. Hutchins BM, Kazane SA, Staflin K, Forsyth JS, Felding-Habermann B, Schultz PG, Smider VV. Site-Specific Coupling and Sterically Controlled Formation of Multimeric Antibody Fab Fragments with Unnatural Amino Acids. *J Mol Biol.* 2011;406:595-603. doi:[10.1016/j.jmb.2011.01.011](https://doi.org/10.1016/j.jmb.2011.01.011)
19. Young DD, Jockush S, Turro NJ, Schultz PG. Synthetase polyspecificity as a tool to modulate protein function. *Bioorg. Med Chem Lett.* 2011;21:7502-04. doi:[10.1016/j.bmcl.2011.09.108](https://doi.org/10.1016/j.bmcl.2011.09.108)
20. Gorduk S. Highly soluble HOPEMP-functionalized phthalocyanines for photodynamic activity: Photophysical, photochemical and aggregation properties. *J Mol Struct.* 2020;1217:128478. doi:[10.1016/j.molstruc.2020.128478](https://doi.org/10.1016/j.molstruc.2020.128478)
21. Eltyshev AK, Minin AS, Smoliuk LT, Benassi E, Belskaya NP. 2-Aryl-2,4-dihydro-5H-[1,2,3]triazolo[4,5-d]pyrimidin-5-ones as a New Platform for the Design and Synthesis of Biosensors and Chemosensors. *Eur J Org Chem.* 2020;2020:316-29. doi:[10.1002/ejoc.201901582](https://doi.org/10.1002/ejoc.201901582)

# Metal-Organic Frameworks for Metal-Ion Batteries: Towards Scalability

Semyon Bachinin, Venera Gilemkhanova, Maria Timofeeva,  
Yuliya Kenzhebayeva, Andrei Yankin \* , Valentin A. Milichko \* 

School of Physics and Engineering, ITMO University, 197101, St. Petersburg, Russia

\* Corresponding authors: [andrei.yankin@metalab.ifmo.ru](mailto:andrei.yankin@metalab.ifmo.ru), [v.milichko@metalab.ifmo.ru](mailto:v.milichko@metalab.ifmo.ru)

This article belongs to the regular issue.

© 2021, The Authors. This article is published in open access form under the terms and conditions of the Creative Commons Attribution (CC BY) license (<http://creativecommons.org/licenses/by/4.0/>).



## Abstract

Metal-organic frameworks (MOFs), being a family of highly crystalline and porous materials, have attracted particular attention in material science due to their unprecedented chemical and structural tunability. Next to their application in gas adsorption, separation, and storage, MOFs also can be utilized for energy transfer and storage in batteries and supercapacitors. Based on recent studies, this review describes the latest developments about MOFs as structural elements of metal-ion battery with a focus on their industry-oriented and large-scale production.

## Keywords

metal-organic frameworks  
batteries  
spin coating  
vapour deposition

Received: 30.07.2021

Revised: 23.08.2021

Accepted: 25.08.2021

Available online: 27.08.2021

## 1. Introduction

Global energy consumption is growing every year, which is associated with active social and economic development. However, limited natural energy resources and climatic changes, caused by their extraction and use, call into question the previous pace of development. In this sense, the development of new green technologies that ensure the energy storage in batteries and energy transfer in an environmentally friendly way is becoming more relevant than ever. Global industrial auto giants such as Mercedes also support such transition to green energy. Despite unprecedented successes in the development of such batteries and accumulators, chemical and physical limitations of existing (organic, inorganic and hybrid) materials yet hinder the wide commercial application and require new solutions in material science. For instance, limited life of the batteries and their cycle stability, physical and chemical stability of structural elements, limited charge/discharge rates, capacity, as well as recyclability of the batteries [1] are cornerstones of the future technology of the clean energy. In this sense, metal-organic frameworks (MOFs) can be considered as new attractive candidates to meet the requirements of next-generation energy storage devices [2].

Emerged over 20 years ago [3], MOFs have become one of the key materials in chemistry and crystal engineering. Being as a family of highly crystalline and porous materials, MOFs are composed of metal nodes and organic ligands linked by coordination bonds. Their "LEGO" nature

possesses an unlimited structural and compositional versatility, providing the desired chemical and physical properties [4]. Due to synthetic design, MOFs' properties such as crystal structure, porosity, stability, and conductivity can be tailored for specific applications. Therefore, such synthetic versatility of MOFs allows one to optimize the functional properties for energy storage [5], since the needs of each device are different.

Today, MOFs, depending on their designed properties, are utilized as the main structural elements of the batteries (Fig. 1): electrodes, solid-state electrolyte, separator and potentially contacts with the metallic conductivity [6-10]. There are many reviews covering the design [5,11-16] fabrication, operation, limitations, and prospects of specific MOFs as individual structural elements such as cathodes and anodes [17-26], electrolytes and separators [27-30]. However, the problem associated with the creation of scalable MOFs for mass (as BASF, MOF-WORX, and NuMat make [31-34]) and large-scale production with focus on energy applications has not been addressed. Here we discuss the latest developments about MOFs as structural elements of metal-ion battery focusing on their industry-oriented production by thin film technology: spin coating and recently developed chemical vapour deposition.

## 2. Discussion

Generally, metal-ion batteries are composed of three major components: anode and cathode with different chemical potentials, immersed in an ion-conducting and electri-

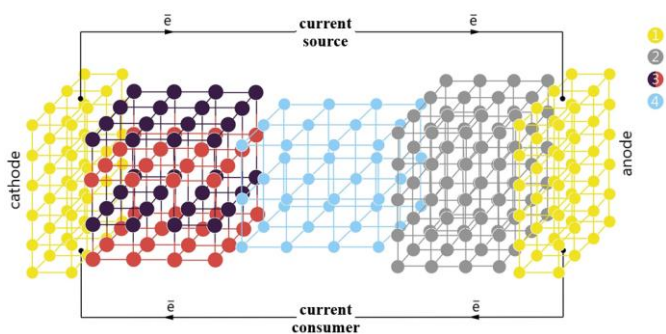


**Fig. 1** Schematic illustration of MOFs (porous coordination polymers) as solid-state electrolytes (4), cathode (3) and anode (2) coating as well as potential electronic conductors (1)

cally insulating electrolyte (Fig. 1). The electrochemical reactions in such batteries are the following: metal ion diffusion within the electrode, charge transfer at the interface between the electrodes and electrolyte, and metal ion transport through the electrolyte. Herein, the recharging of the batteries (i.e. current source) occurs in a “rocking-chair” fashion: metal ions transfer between cathode and anode during charge/discharge cycles (Fig. 1). During discharge (i.e. current consumer), metal ions travel from the anode to the cathode, while electrons move externally from the anode to the cathode.

Metal-organic frameworks demonstrate high potential to optimize the performance of metal-ion batteries. This is facilitated by a number of their distinctive properties such as porosity, redox behavior, various types of conductivity (ionic and electronic), encapsulation of various molecules and ions, etc. Fig. 1 demonstrates a schematic diagram of a metal ion battery with highlighted areas corresponding to MOFs as cathodes, anodes, solid-state electrolytes and separators.

First, we consider MOFs as cathodes and anodes. Generally, metal-organic frameworks are semiconductors in nature, in some cases the band gap reaches up to 5 eV. Nevertheless, there are compounds with the lower band gap possessing hopping electronic conductivity. The mechanisms of electronic transport in MOFs are the following [35-37]: through-bond, through-plane, through-space, redox-hopping, and guest-promoted pathways. This provides an opportunity to utilize ZIF-8 ( $Zn(mIm)_2$ , where  $mIm = 2$ -methylimidazolate), metal-ion batteries, addressing two issues: providing electron transport and insertion/extraction of ions due to redox activity [38-40]. Nam et al. [38] were able to combine these two properties and provide a prototype of the metal-ion battery with a cathode entirely made of two-dimensional MOF ( $Cu_3(HHTP)_2$ , where  $HHTP = 2,3,6,7,10,11$ -hexahydroxytriphenylene) with an electronic conductivity of  $0.2 S cm^{-1}$  (Fig. 2a). Also, Li et al. [40] demonstrated similar approach, but for the anode (Fig. 2b).

Deposition of metal-organic frameworks on the anodes also allows one to improve the capacitive characteristics of metal-ion batteries due to insertion/extraction of various ions through the MOF layer. This makes it possible to increase the effective anode area without changing the dimensional characteristics of the device, which, in its turn, promises miniaturization of existing batteries. A number of papers [41-48], considering such an approach, demonstrate the achievement of significant results in current densities, charge capacity, and cyclic stability. The mechanism of insertion/extraction of ions is also described in details in [44] using the example of aluminum-based MOF (Fig. 3). In addition, the deposition of MOFs on the cathodes possesses the similar effect, which has been considered by the authors of [48-52].

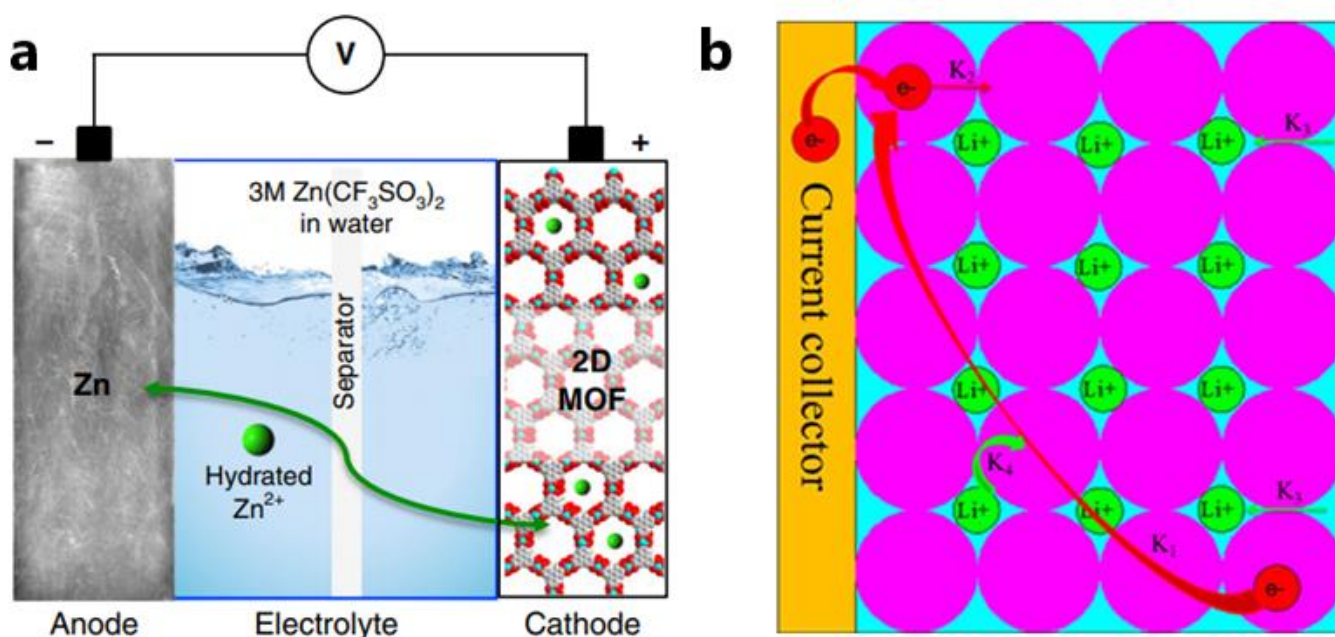


**Fig. 2** The concept for the MOF as a cathode (a) [38] and anode (b) [40]

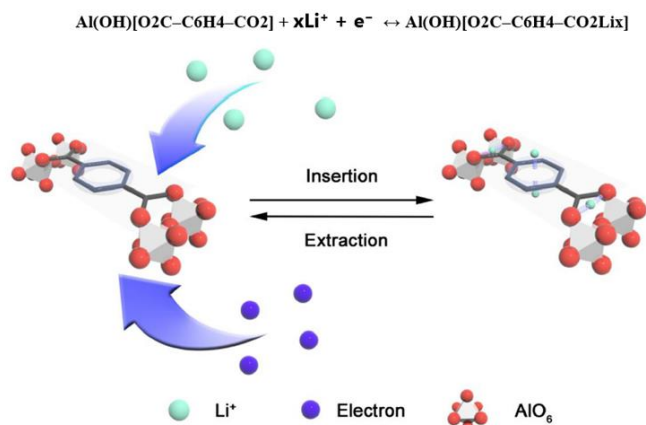


**Fig. 3** The mechanism of insertion/extraction of various ions through MOF layer [44]

Utilization of metal-organic frameworks as an active medium for ion transport is the other side of the story. The porous structure provides ion transport through the MOF, which allows one to consider it as a solid-state electrolyte [53-59]. The reason to use MOF as a solid-state electrolyte is dictated, first, by a decrease in the toxicity of the resulting metal-ion batteries. Indeed, the common liquid electrolytes are extremely toxic, which makes the process of disposal quite difficult and expensive. Such toxicity also makes existing batteries extremely unsafe for use in electronic devices for children. In this sense, the transition from the liquid electrolytes towards solid-state ones can improve this issue and allows the batteries to be recyclable. In addition, a number of metal-organic frameworks demonstrate promising operation characteristics under the extreme conditions: high temperatures,

mechanical stress, directed thermal action, etc. A number of recent research works [54-59] prove the validity of this suggestions through the embedding of metal-organic frameworks as an additional layer [58] (Fig. 4c) or making the energy device based on MOF as an active layer [57] (Fig. 4a,b). Also, a review of potentially suitable compositions of MOFs as solid-state electrolytes can be found in [59].

The increasing focus on industrially applicable MOFs [31-34] for microelectronics and energy applications highlights significant limitations of common solution methods and emphasizes the need for more scalable technologies like Roll-on approach, which is highly needed for production of portable batteries. The possibility of the scaling of the synthesis of functional MOFs is directly related to the development of technologies for the growth of high-quality crystals in the form of thin films. To address this issue, first, we consider spin coating approach [60-64]. This is one of the simplest methods for MOF scalability allowing the deposition of MOF films on different rigid and flexible substrates (metal, semiconductor or dielectric) with different morphologies. The method consists of the interaction of droplets of two solutions (an organic ligand and a metal salt) on the surface of a rotating substrate (Fig. 5a) [60]. Due to the high rotation speeds of the substrate, the resulting film has relatively good uniformity in thickness and composition (Fig. 5b).

The heating of the substrate can be also applied to increase both the rate of synthesis and the crystallinity. The authors of [61] obtained a 150 nm film on an aluminum electrode at a rotation speed of 3000 rpm and a substrate temperature of 140 °C, which can potentially

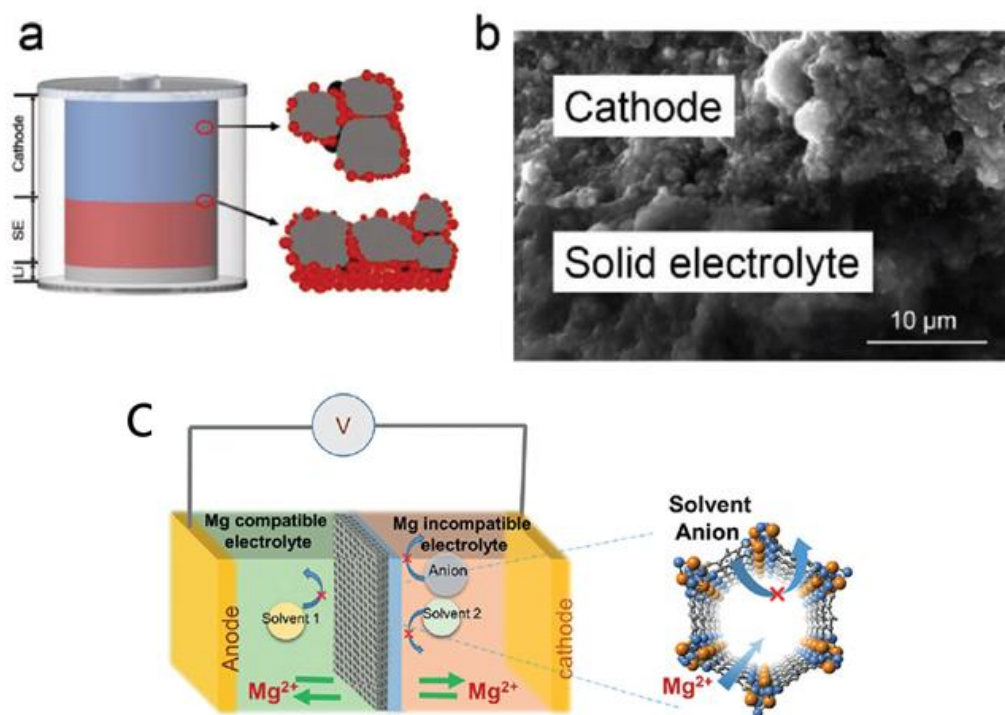


**Fig. 4** MOF as a solid-state electrolyte (a,b) [57] and separator film (c) [58]

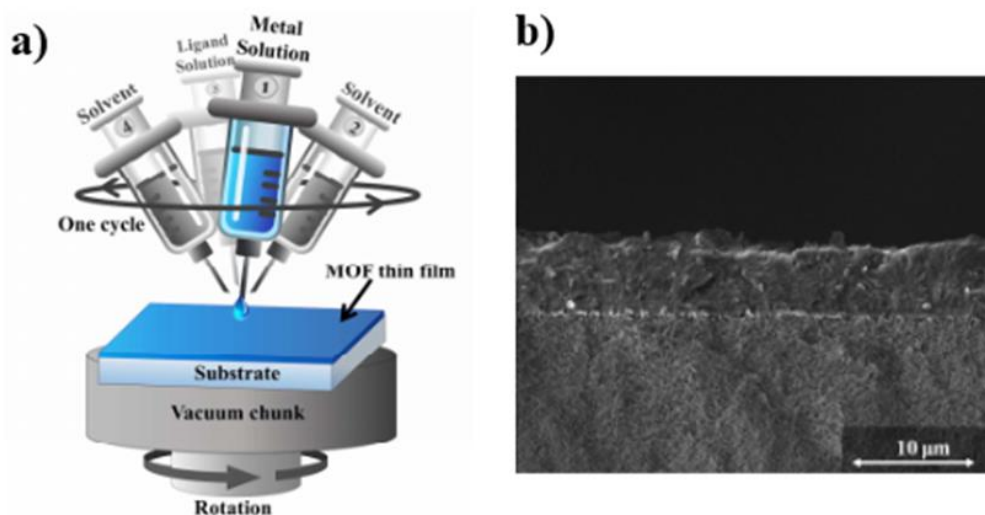


**Fig. 5** Schematic illustration of spin-coating approach (a) and cross-section view of MOF thin film obtained by scanning electron microscopy (b) [60]

be used for the process of modifying the electrodes of metal-ion batteries. Chen et al. [62] also showed the possibility of spin-coating the flexible film with an electronic type of conductivity, which is interesting as electrode layers in the device of metal-ion batteries. Also, direct evidence of the validity of the spin-coating technology application follows from the paper [63] where Fan et al. modified the surface of the Zn-MOF anode by centrifugation. Finally, considering the battery, whose structure consists of multilayer MOFs as electrodes, electrolytes and separators (Fig. 1), the specific technology is required. In this sense, the spin-coating makes it possible to fabricate such multilayer structures, as evidenced by the results obtained in [64].

Next highly promising approach is chemical vapour deposition (CVD) [65-74]. Indeed, CVD as a non-solvent method is a well-known industrial approach for obtaining surfaces suitable for micro- and optoelectronics since the corrosion and contamination issues are solved. A variant of CVD, MOCVD (metal-organic CVD) is a standard process for laser diode, LED, and semiconductor manufacturing, meaning it can be used for MOF synthesis, as well. Following the research works on MOF CVD, common structures such as ZIF-8, ZIF-67 ( $\text{Co}(\text{mIm})_2$ , where  $\text{mIm}$  = 2-methylimidazolate), HKUST-1 ( $\text{Cu}_3(\text{BTC})_2$ , where  $\text{BTC}$  = benzene-1,3,5-tricarboxylic acid) and MIL-53 ( $\text{Al-BDC}$ , where  $\text{BDC}$  = 1,4 benzene dicarboxylic acid), recently utilized for energy storage [21], can be prepared as model thin films. However, in contrast to solution chemistry, the limited possibilities of CVD for using a variable concentration of various solvents significantly limit the resulting MOF topologies, while it is not an insurmountable problem for the method.

The general concept of MOF CVD is illustrated in Fig. 6. Rob Ameloot and co-workers describe this method as a two-step procedure [65]: the deposition of the metal oxide layer on a support by, for instance, atomic layer deposition (ALD), followed by the exposure of this oxide coating

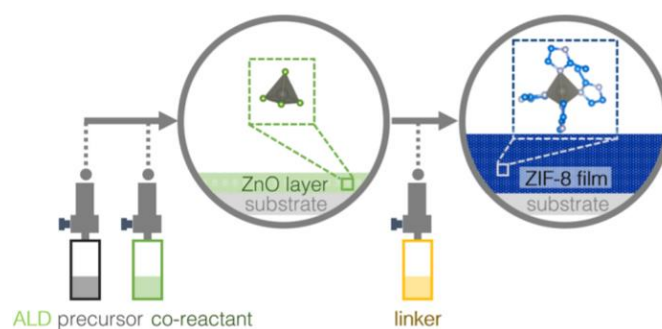


**Fig. 6** Schematic illustration of MOF CVD process [68]

to a vaporized linker resulting in a vapor-solid reaction towards the formation of the desired MOF structures. Following this approach, ZIF-8 films were obtained by Stassen et al. [65]. ZIF-8 was deposited on silicon pillars with a 25:1 aspect ratio by vapour-solid transformation of 25 nm ALD zinc oxide films. It is vital to mention the possibility of obtaining conformal coatings by such approach on various, often fragile, surfaces. Intriguing, the presence of water during synthesis promotes formation of a non-porous diamondoid  $\text{Zn}(\text{mIm})_2$  polymorph, but under high temperatures the water evaporation eliminates the chances of amorphous material to form.

Similar effect of lack of solvent has been demonstrated by Han et al. [66] who reported solvent-free HKUST-1 film deposition under vacuum conditions. They combined CVD and physical vapour deposition processes using layer-by-layer (LBL) growth where after each  $\text{H}_3\text{BTC}$  deposition cycle a monolayer Cu was grown again.

The group of Ameloot [67] also reported the growth of MOF based on Cu(II) and linkers 1,4-benzenedicarboxylic acid ( $\text{H}_2\text{BDC}$ ) and trans-1,4-cyclohexanedicarboxylic acid ( $\text{H}_2\text{CDC}$ ). The MOF-CVD method for these materials consists of two steps: vapour-phase deposition of copper or copper oxide films as a metal source, and a solid-vapour reaction between this precursor and the vaporised organic linker. It is important to note that depending on synthesis

conditions (dry or humid) diverse MOFs' structures were obtained. For  $H_2CDC$  linker humidity did not play a major role and porous  $CuCDC$  was normally formed. However, for  $H_2BDC$  linker, depending on the humidity level,  $CuBDC$  or  $CP-CuBDC$  structure similar to coordination polymer  $[Cu_2(OH)_2(BDC)]$  could be obtained.

A number of emerging problems in the process of MOF-CVD, such as the incomplete conversion of the metal-oxide precursor to MOF, and the degradation of the organic ligand during deposition at elevated temperature were described [68-71]. A possible solution was proposed by Cruz et al. [68]: involving an increase of exposure time and decrease of the thickness of the metal-oxide precursor. Furthermore, the use of low-temperature synthesis (80 °C) conditions to circumvent these challenges was explored for MAF-6 ( $RHO-Zn(eIm)_2$ , where  $eIm = 2$ -ethylimidazolate) [69], MAF-252 ( $Zn(dpt)_2$ , where  $dpt = 3$ -(2-pyridyl)-5-(4-pyridyl)-1,2,4-triazolate)) [70] (Fig. 7), ZIF-8 and ZIF-67 [71] structures.

Another issue comes from MOF-CVD method itself that allows obtaining MOFs with limited porosity [65-71]. This deteriorates a whole range of functional properties including ion transport. This issue can be overcome by accounting for the following factors [67,68]: (i) humidity has to be controlled since it can increase chances of amorphous intermediate formation, thus, affecting thin film roughness – the more humid conditions are, the rougher are the films produced; (ii) the thickness of metal-oxide precursor has to be controlled in order to fully convert it into MOF. Otherwise, it acts as a protecting shell that hampers further MOF growth. So far, only model MOFs with relatively simple topologies and short ligands have been synthesized by CVD, therefore, leaving room for further investigations of MOFs with more complex hierarchy and variable ion/electron conductivity.

The report by Stassin et al. [72] creates a basis for the direct comparison of the solvothermal and vapour deposition methods for the synthesis of functional and polymorphic MOFs. MOFs Al-MIL-53-Fum and Al-MIL-53-Mes (Al-MIL-68-Mes) were synthesized with and without modulators. When formic acid was used as a modulator, MOF crystallized at 80 °C by CVD in the orthorhombic crystal system with  $Pnma$  space group. At the same time, modula-

tor-free product crystallized by solvothermal method in the monoclinic space group  $P21/c$ . The change of the modulator from formic to mesaconic acid led to formation of Al-MIL-53-Mes by CVD that crystallizes in the orthorhombic with  $Pnma$  space group. This work highlighted the principle possibility of the controlled synthesis of structurally diverse compounds via conscious vapour deposition synthesis.

Similar message was conveyed by a very recent work by Tu et al. [73], which described another approach to controlled MOF-CVD synthesis by using the so-called template vapor that arranges the MOF building blocks and promotes the formation of desired product. They found out that the reaction between zinc oxide and 4,5-dichloroimidazole (HdcIm) leads to the formation of either porous kinetic phase ZIF-71 [ $Zn(dcim)_2$ ] ( $dcim = 4,5$ -dichloroimidazolate) with RHO topology, or thermodynamically stable phase ZIF-72 (the same chemical formula as ZIF-71) with LCS topology. The addition of template vapors enabled formation of ZIF-71 at lower temperatures (120 °C vs 160 °C); however, at temperatures above 120 °C it was impossible to avoid the phase transition from ZIF-71 to ZIF-72.

### 3. Conclusions

Conventional solution chemistry certainly remain the key approach for the synthesis of MOFs for diverse applications including electrochemical energy storage [74]. However, the increasing focus on industrially applicable MOFs [31-34] for microelectronics, optics [75] and energy application highlight significant limitations of the solution methods and emphasizes the need for more scalable and industry-oriented technologies. Here, we cover advanced methods, such as spin coating and vapour deposition techniques, allowing large-scale and fast productions of functional MOFs. These industrially oriented and scalable methods demonstrate high potential for producing the functional MOF thin films. Specifically, the CVD technique appears as the most optimal and promising method for the industrial manufacture of MOFs. The intense research during the past 5 years identified a number of technological challenges hampering the implementation of MOF-CVD and indicated avenues for their solution. The key challenges include the incomplete conversion of the metal-oxide precursor to MOF, the degradation of the organic ligand during deposition at elevated temperature [68-71], as well as growth of MOFs with limited porosity [65-71]. All these issues can potentially be addressed. Also, over the past year, the possibility of large-scale growth of MOFs with a structural diversity has been also demonstrated [73,74], which, we believe, will be one of the driving forces in MOF crystal engineering in the near future.

Concerning spin coating approach, there are still technological problems of MOF thin film fabrication such as a poorly controlled growth process, the influence of external

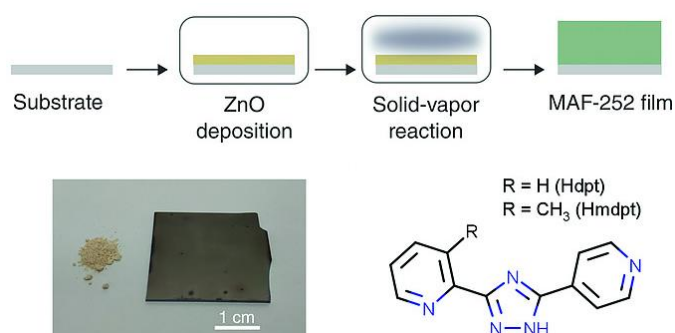


**Fig. 7** The scheme of MAF-252 thin film fabrication with corresponding optical images of MAF-252 powder and large-scale film [70]

factors (mechanical vibrations, convection flows and insufficient automation), and a limited list of structural elements (especially ligands) involved in the crystal growth. The latter is associated with the high growth rate of thin films during the spin coating, which does not allow sufficiently large ligands (porphyrins, TBAPY etc.) to organize a porous periodic lattice. Finally, inhomogeneity of the film (domain structure) and a high degree of surface roughness limit the applicability of the method.

In our review, we also omitted the other industrially oriented methods for scalable MOF fabrication, such as electrochemistry, mechanochemistry and microwave-assisted synthesis. The reason for this is the rather high degree of development of these methods, which is reflected in the relevant reviews [76-81].

## Acknowledgments

The authors acknowledge the financial support from the Russian Foundation for Basic Research (Project No. 20-13-50454).

## References

- Nguyen TP, Easley AD, Kang N, Khan S, Lim SM, Rezenom YH, Wooley KL. Polypeptide organic radical batteries. *Nature*. 2021;593(7857):61-6. doi:[10.1038/s41586-021-03399-1](https://doi.org/10.1038/s41586-021-03399-1)
- Xu G, Nie P, Dou H, Ding B, Li L, Zhang X. Exploring metal organic frameworks for energy storage in batteries and supercapacitors. *Materials Today*. 2017;20(4):191-209. doi:[10.1016/j.mattod.2016.10.003](https://doi.org/10.1016/j.mattod.2016.10.003)
- Li H, Eddaoudi M, O'Keeffe M, Yaghi OM. Design and synthesis of an exceptionally stable and highly porous metal-organic framework. *Nature*. 1999;402(6759):276-79. doi:[10.1038/46248](https://doi.org/10.1038/46248)
- Mezenov YA, Krasilin AA, Dzyuba VP, Nominé A, Milichko VA. Metal-organic frameworks in modern physics: Highlights and perspectives. *Advanced Science*. 2019;6(17):1900506. doi:[10.1002/advs.201900506](https://doi.org/10.1002/advs.201900506)
- Baumann AE, Burns DA, Liu B, Thoi VS. Metal-organic framework functionalization and design strategies for advanced electrochemical energy storage devices. *Communications Chemistry*. 2019;2(1):1-14. doi:[10.1038/s42004-019-0184-6](https://doi.org/10.1038/s42004-019-0184-6)
- Xie LS, Skorupskii G, Dincă M. Electrically conductive metal-organic frameworks. *Chemical reviews*. 2020;120(16):8536-80. doi:[10.1021/acs.chemrev.9b00766](https://doi.org/10.1021/acs.chemrev.9b00766)
- Dou JH, Sun L, Ge Y, Li W, Hendon CH, Li J, Dincă M. Signature of metallic behavior in the metal-organic frameworks M<sub>3</sub> (hexaiminobenzene) 2 (M = Ni, Cu). *Journal of the American Chemical Society*. 2017;139(39):13608-11. doi:[10.1021/jacs.7b07234](https://doi.org/10.1021/jacs.7b07234)
- Clough AJ, Orchanian NM, Skelton JM, Neer AJ, Howard SA, Downes CA, Marinescu SC. Room Temperature Metallic Conductivity in a Metal-Organic Framework Induced by Oxidation. *Journal of the American Chemical Society*. 2019;141(41):16323-30. doi:[10.1021/jacs.9b06898](https://doi.org/10.1021/jacs.9b06898)
- He Y, Cubuk ED, Allendorf MD, Reed EJ. Metallic metal-organic frameworks predicted by the combination of machine learning methods and ab initio calculations. *The journal of physical chemistry letters*. 2018;9(16):4562-9. doi:[10.1021/acs.jpcclett.8b01707](https://doi.org/10.1021/acs.jpcclett.8b01707)
- Foster ME, Sohlberg K, Allendorf MD, Talin AA. Unraveling the semiconducting/metallic discrepancy in Ni<sub>3</sub> (HITP) 2. *The journal of physical chemistry letters*. 2018;9(3):481-6. doi:[10.1021/acs.jpcclett.7b03140](https://doi.org/10.1021/acs.jpcclett.7b03140)
- Zhong M, Kong L, Zhao K, Zhang YH, Li N, Bu XH. Recent Progress of Nanoscale Metal-Organic Frameworks in Synthesis and Battery Applications. *Advanced Science*. 2021;8(4):2001980. doi:[10.1002/advs.202001980](https://doi.org/10.1002/advs.202001980)
- Zheng ZJ, Ye H, Guo ZP. Recent progress on pristine metal/covalent-organic frameworks and their composites for lithium-sulfur batteries. *Energy & Environmental Science*. 2021;14(4):1835-53. doi:[10.1039/DoEE03181J](https://doi.org/10.1039/DoEE03181J)
- Thakur AK, Majumder M, Patole SP, Zaghbi K, Reddy MV. Metal-organic framework-based materials: advances, exploits, and challenges in promoting post Li-ion battery technologies. *Materials Advances*. 2021;2(8):2457-82. doi:[10.1039/DoMA01019G](https://doi.org/10.1039/DoMA01019G)
- Wen X, Zhang Q, Guan J. Applications of metal-organic framework-derived materials in fuel cells and metal-air batteries. *Coordination Chemistry Reviews*. 2020;409:213214. doi:[10.1016/j.ccr.2020.213214](https://doi.org/10.1016/j.ccr.2020.213214)
- Sun W, Tang X, Wang Y. Multi-metal-organic frameworks and their derived materials for Li/Na-ion batteries. *Electrochemical Energy Reviews*. 2020;3(1):127-54. doi:[10.1007/s41918-019-00056-0](https://doi.org/10.1007/s41918-019-00056-0)
- Mehtab T, Yasin G, Arif M, Shakeel M, Korai RM, Nadeem M, Lu X. Metal-organic frameworks for energy storage devices: batteries and supercapacitors. *Journal of Energy Storage*. 2019;21:632-46. doi:[10.1016/j.est.2018.12.025](https://doi.org/10.1016/j.est.2018.12.025)
- Du J, Li F, Sun L. Metal-organic frameworks and their derivatives as electrocatalysts for the oxygen evolution reaction. *Chemical Society Reviews*. 2021;4461(4):214118. doi:[10.1039/DoCS01191F](https://doi.org/10.1039/DoCS01191F)
- Yan R, Ma T, Cheng M, Tao X, Yang Z, Ran F, Yang W. Metal-Organic-Framework-Derived Nanostructures as Multifaceted Electrodes in Metal-Sulfur Batteries. *Advanced Materials*. 2021;33(27):2008784. doi:[10.1002/adma.202008784](https://doi.org/10.1002/adma.202008784)
- Zhu W, Li A, Wang Z, Yang J, Xu Y. Metal-Organic Frameworks and Their Derivatives: Designing Principles and Advances toward Advanced Cathode Materials for Alkali Metal Ion Batteries. *Small*. 2021;17(22):2006424. doi:[10.1002/smll.202006424](https://doi.org/10.1002/smll.202006424)
- Jiang Y, Zhao H, Yue L, Liang J, Li T, Liu Q, Sun X. Recent advances in lithium-based batteries using metal organic frameworks as electrode materials. *Electrochemistry Communications*. 2020;22:106881. doi:[10.1016/j.elecom.2020.106881](https://doi.org/10.1016/j.elecom.2020.106881)
- Zhao R, Liang Z, Zou R, Xu Q. Metal-organic frameworks for batteries. *Joule*. 2018;2(11):2235-59. doi:[10.1016/j.joule.2018.09.019](https://doi.org/10.1016/j.joule.2018.09.019)
- Reddy RCK, Lin J, Chen Y, Zeng C, Lin X, Cai Y, Su CY. Progress of nanostructured metal oxides derived from metal-organic frameworks as anode materials for lithium-ion batteries. *Coordination Chemistry Reviews*. 2020;420:213434. doi:[10.1016/j.ccr.2020.213434](https://doi.org/10.1016/j.ccr.2020.213434)
- Wu Q, Zhou X, Xu J, Cao F, Li C. Carbon-based derivatives from metal-organic frameworks as cathode hosts for Li-S batteries. *Journal of Energy Chemistry*. 2019;38:94-113. doi:[10.1016/j.jechem.2019.01.005](https://doi.org/10.1016/j.jechem.2019.01.005)
- Wang ZY, Tao HZ, Yue Y. Metal-organic-framework-based cathodes for enhancing the electrochemical performances of batteries: a review. *ChemElectroChem*. 2019;6(21):5358-74. doi:[10.1002/celec.201900843](https://doi.org/10.1002/celec.201900843)
- Shrivastav V, Sundriyal S, Goel P, Kaur H, Tuteja SK, Vikrant K, Deep A. Metal-organic frameworks (MOFs) and their composites as electrodes for lithium battery applications: Novel means for alternative energy storage. *Coordination Chemistry Reviews*. 2019;393:48-78. doi:[10.1016/j.ccr.2019.05.006](https://doi.org/10.1016/j.ccr.2019.05.006)

26. Zhang L, Liu H, Shi W, Cheng P. Synthesis strategies and potential applications of metal-organic frameworks for electrode materials for rechargeable lithium ion batteries. *Coordination Chemistry Reviews*. 2019;388:293-309. doi:[10.1016/j.ccr.2019.02.030](https://doi.org/10.1016/j.ccr.2019.02.030)
27. Barbosa J, Gonçalves RF, Costa CM, de Zea Bermudez V, Fidalgo A, Zhang Q, Lanceros-Mendez S. Metal-organic frameworks and zeolite materials as active fillers for lithium-ion battery solid polymer electrolytes. *Materials Advances*. 2021;2(12):3790-805. doi:[10.1039/D1MA00244A](https://doi.org/10.1039/D1MA00244A)
28. Huang WH, Li XM, Yang XF, Zhang XX, Wang HH, Wang H. The recent progress and perspectives on metal-and covalent-organic framework based solid-state electrolytes for lithium-ion batteries. *Materials Chemistry Frontiers*. 2021;5(9):3593-613. doi:[10.1039/DOQM00936A](https://doi.org/10.1039/DOQM00936A)
29. Chu Z, Gao X, Wang C, Wang T, Wang G. Metal-organic frameworks as separators and electrolytes for lithium-sulfur batteries. *Journal of Materials Chemistry A*. 2021;9(12):7301-16. doi:[10.1039/DO1A11624F](https://doi.org/10.1039/DO1A11624F)
30. Chen T, Chen S, Chen Y, Zhao M, Losic D, Zhang S. Metal-organic frameworks containing solid-state electrolytes for lithium metal batteries and beyond. *Materials Chemistry Frontiers*. 2021;5(4):1771-94. doi:[10.1039/DOQM00856g](https://doi.org/10.1039/DOQM00856g)
31. Furukawa H, Müller U, Yaghi OM. "Heterogeneity within order" in metal-organic frameworks. *Angewandte Chemie International Edition*. 2015;54(11):3417-30. doi:[10.1002/anie.201410252](https://doi.org/10.1002/anie.201410252)
32. Ren J, Dyosiba X, Musyoka NM, Langmi HW, Mathe M. Review on the current practices and efforts towards pilot-scale production of metal-organic frameworks (MOFs). *Coordination Chemistry Reviews*. 2017;352:187-219. doi:[10.1016/j.ccr.2017.09.005](https://doi.org/10.1016/j.ccr.2017.09.005)
33. Silva P, Vilela SMF, Tome JPC, Almeida Paz FA. Multifunctional metal-organic frameworks: from academia to industrial applications. *Chemistry Society Reviews*. 2015;44:6774-803. doi:[10.1039/C5CS00307e](https://doi.org/10.1039/C5CS00307e)
34. Rubio-Martinez M, Avci-Camur C, Thornton AW, Imaz I, MasPOCH D, Hill MR. New synthetic routes towards MOF production at scale. *Chemical Society Reviews*. 2017;46(11):3453-80. doi:[10.1039/C7CS00109f](https://doi.org/10.1039/C7CS00109f)
35. Johnson EM, Ilic S, Morris AJ. Design Strategies for Enhanced Conductivity in Metal-Organic Frameworks. *ACS Central Science*. 2021;7(3):445-53. doi:[10.1021/acscentsci.1c00047](https://doi.org/10.1021/acscentsci.1c00047)
36. Liu J, Song X, Zhang T, Liu S, Wen H, Chen L. 2D Conductive Metal-Organic Frameworks: An Emerging Platform for Electrochemical Energy Storage. *Angewandte Chemie International Edition*. 2021;60(11):5612-24. doi:[10.1002/anie.202006102](https://doi.org/10.1002/anie.202006102)
37. Day RW, Bediako DK, Rezaee M, Parent LR, Skorupskii G, Arguilla MQ, Dincă M. Single crystals of electrically conductive two-dimensional metal-organic frameworks: Structural and electrical transport properties. *ACS central science*. 2019;5(12):1959-64. doi:[10.1021/acscentsci.9b01006](https://doi.org/10.1021/acscentsci.9b01006)
38. Nam KW, Park SS, dos Reis R. et al. Conductive 2D metal-organic framework for high-performance cathodes in aqueous rechargeable zinc batteries. *Nature Community*. 2019;10:4948. doi:[10.1038/s41467-019-12857-4](https://doi.org/10.1038/s41467-019-12857-4)
39. Gu S, Bai Z, Majumder S, Huang B, Chen G. Conductive metal-organic framework with redox metal center as cathode for high rate performance lithium ion battery. *Journal of Power Sources*. 2019;429:22-9. doi:[10.1016/j.jpowsour.2019.04.087](https://doi.org/10.1016/j.jpowsour.2019.04.087)
40. Li Z, Huang X, Sun C, Chen X, Hu J, Stein A, Tang B. Thin-film electrode based on zeolitic imidazolate frameworks (ZIF-8 and ZIF-67) with ultra-stable performance as a lithium-ion battery anode. *Journal of Materials Science*. 2017;52:3979-91. doi:[10.1007/s10853-016-0660-7](https://doi.org/10.1007/s10853-016-0660-7)
41. Luo Y, Wu M, Pang B, Ge J, Li R, Zhang P, Okada S. Metal-organic Framework of [Cu<sub>2</sub> (BIPA-TC)(DMA) 2] n: A Promising Anode Material for Lithium-Ion Battery. *ChemistrySelect*. 2020;5(14):4160-4. doi:[10.1002/slct.202000503](https://doi.org/10.1002/slct.202000503)
42. Weng YG, Yin WY, Jiang M, Hou JL, Shao J, Zhu QY, Dai J. Tetrathiafulvalene-Based Metal-Organic Framework as a High-Performance Anode for Lithium-Ion Batteries. *ACS Applied Materials & Interfaces*. 2020;12(47):52615-23. doi:[10.1021/acsami.0c14510](https://doi.org/10.1021/acsami.0c14510)
43. Han Y, Qi P, Zhou J, Feng X, Li S, Fu X, Wang B. Metal-organic frameworks (MOFs) as sandwich coating cushion for silicon anode in lithium ion batteries. *ACS applied materials & interfaces*. 2015;7(48):26608-13. doi:[10.1021/acsami.5b08109](https://doi.org/10.1021/acsami.5b08109)
44. Gao C, Wang P, Wang Z, Kær SK, Zhang Y, Yue Y. The disordering-enhanced performances of the Al-MOF/graphene composite anodes for lithium ion batteries. *Nano Energy*. 2019;65:104032. doi:[10.1016/j.nanoen.2019.104032](https://doi.org/10.1016/j.nanoen.2019.104032)
45. Zhao G, Tang L, Zhang L, Chen X, Mao Y, Sun K. Well-developed capacitive-capacity of metal-organic framework derived Co<sub>3</sub>O<sub>4</sub> films in Li ion battery anodes. *Journal of Alloys and Compounds*. 2018;746:277-84. doi:[10.1016/j.jallcom.2018.02.285](https://doi.org/10.1016/j.jallcom.2018.02.285)
46. Mutahir S, Wang C, Song J, Wang L, Lei W, Jiao X, Hao Q. Pristine Co (BDC) TEDo. 5 a pillared-layer biligand cobalt based metal organic framework as improved anode material for lithium-ion batteries. *Applied Materials Today*. 2020;21:100813. doi:[10.1016/j.apmt.2020.100813](https://doi.org/10.1016/j.apmt.2020.100813)
47. Wang J, Dong S, Zhang Y, Chen Z, Jiang S, Wu L, Zhang X. Metal-organic framework derived titanium-based anode materials for lithium ion batteries. *Nano-Structures & Nano-Objects*. 2018;15:48-53. doi:[10.1016/j.nanoso.2018.03.004](https://doi.org/10.1016/j.nanoso.2018.03.004)
48. Li H, Lang J, Lei S, Chen J, Wang K, Liu L, Yan X. A High-Performance Sodium-Ion Hybrid Capacitor Constructed by Metal-Organic Framework-Derived Anode and Cathode Materials. *Advanced Functional Materials*. 2018;28(30):1800757. doi:[10.1002/adfm.201800757](https://doi.org/10.1002/adfm.201800757)
49. Nagarathinam M, Saravanan K, Phua EJH, Reddy MV, Chowdari BVR, Vittal JJ. Redox-Active Metal-Centered Oxalato Phosphate Open Framework Cathode Materials for Lithium Ion Batteries. *Angewandte Chemie International Edition*. 2012;51(24):5866-70. doi:[10.1002/anie.201200210](https://doi.org/10.1002/anie.201200210)
50. Zou F, Liu K, Cheng CF, Ji Y, Zhu, Y. Metal-organic frameworks (MOFs) derived carbon-coated NiS nanoparticles anchored on graphene layers for high-performance Li-S cathode material. *Nanotechnology*. 2020;31(48):485404. doi:[10.1088/1361-6528/aba9b](https://doi.org/10.1088/1361-6528/aba9b)
51. Xue R, Liu N, Bao L, Chen L, Su Y, Lu Y, Wu F. UiO-66 type metal-organic framework as a multifunctional additive to enhance the interfacial stability of Ni-rich layered cathode material. *Journal of Energy Chemistry*. 2020;50:378-86. doi:[10.1016/j.jechem.2020.03.049](https://doi.org/10.1016/j.jechem.2020.03.049)
52. Shimizu T, Wang H, Matsumura D, Mitsuhara K, Ohta T, Yoshikawa H. Porous Metal-Organic Frameworks Containing Reversible Disulfide Linkages as Cathode Materials for Lithium-Ion Batteries. *ChemSusChem*. 2020;13(9):2256-22. doi:[10.1002/cssc.201903471](https://doi.org/10.1002/cssc.201903471)
53. Sadakiyo M, Kitagawa H. Ion-conductive metal-organic frameworks. *Dalton Transactions*. 2021;50(16):5385-97. doi:[10.1039/DO1T04384B](https://doi.org/10.1039/DO1T04384B)
54. Wiers BM, Foo ML, Balsara NP, Long JR. A solid lithium electrolyte via addition of lithium isopropoxide to a metal-organic framework with open metal sites. *Journal of the American Chemical Society*. 2011;133(37):14522-5. doi:[10.1021/ja205827z](https://doi.org/10.1021/ja205827z)
55. Fujie K, Ikeda R, Otsubo K, Yamada T, Kitagawa H. Lithium ion diffusion in a metal-organic framework mediated by an ionic liquid. *Chemistry of Materials*. 2015;27(21):7355-61. doi:[10.1021/acs.chemmater.5b02986](https://doi.org/10.1021/acs.chemmater.5b02986)

56. Park SS, Tulchinsky Y, Dincă M. Single-ion Li<sup>+</sup>, Na<sup>+</sup>, and Mg<sup>2+</sup> solid electrolytes supported by a mesoporous anionic Cu-azolate metal-organic framework. *Journal of the American Chemical Society*. 2017;139(38):13260-3. doi:[10.1021/jacs.7b06197](https://doi.org/10.1021/jacs.7b06197)
57. Wu JF, Guo X. Nanostructured Metal-Organic Framework (MOF)-Derived Solid Electrolytes Realizing Fast Lithium Ion Transportation Kinetics in Solid-State Batteries. *Small*. 2019;15(5):1804413. doi:[10.1002/smll.201804413](https://doi.org/10.1002/smll.201804413)
58. Luo J, Li Y, Zhang H, Wang A, Lo WS, Dong Q, Wang D. A metal-organic framework thin film for selective Mg<sup>2+</sup> transport. *Angewandte Chemie International Edition*. 2019;58(43):15313-17. doi:[10.1002/anie.201908706](https://doi.org/10.1002/anie.201908706)
59. Kinik FP, Uzun A, Keskin S. Ionic liquid/metal-organic framework composites: from synthesis to applications. *ChemSusChem*. 2017;10(14):2842-63. doi:[10.1002/cssc.201700716](https://doi.org/10.1002/cssc.201700716)
60. Chernikova V, Shekhah O, Eddaoudi M. Advanced fabrication method for the preparation of MOF thin films: Liquid-phase epitaxy approach meets spin coating method. *ACS applied materials & interfaces*. 2016;8(31):20459-64. doi:[10.1021/acsami.6b04701](https://doi.org/10.1021/acsami.6b04701)
61. Gutierrez M, Martín C, Souza BE, Van der Auweraer M, Hofkens J, Tan JC. Highly luminescent silver-based MOFs: Scalable eco-friendly synthesis paving the way for photonic sensors and electroluminescent devices. *Applied Materials Today*. 2020;21:100817. doi:[10.1016/j.apmt.2020.100817](https://doi.org/10.1016/j.apmt.2020.100817)
62. Chen X, Lu Y, Dong J, Ma L, Yi Z, Wang Y, Liu Y. Ultrafast In Situ Synthesis of Large-Area Conductive Metal-Organic Frameworks on Substrates for Flexible Chemiresistive Sensing. *ACS Applied Materials & Interfaces*. 2020;12(51):57235-44. doi:[10.1021/acsami.0c18422](https://doi.org/10.1021/acsami.0c18422)
63. Fan L, Guo Z, Zhang Y, Wu X, Zhao C, Sun X, Zhang N. Stable artificial solid electrolyte interphase films for lithium metal anode via metal-organic frameworks cemented by polyvinyl alcohol. *Journal of Materials Chemistry A*. 2020;8(1):251-8. doi:[10.1039/c9ta10405d](https://doi.org/10.1039/c9ta10405d)
64. Gutierrez M, Martín C, Souza BE, Van der Auweraer M, Hofkens J, Tan JC. Highly luminescent silver-based MOFs: Scalable eco-friendly synthesis paving the way for photonic sensors and electroluminescent devices. *Applied Materials Today*. 2020;21:100817. doi:[10.1016/j.apmt.2020.100817](https://doi.org/10.1016/j.apmt.2020.100817)
65. Stassen I, Styles M, Grecni G, Van Gorp H, Vanderlinden W, De Feyter S, Ameloot R. Chemical vapour deposition of zeolitic imidazolate framework thin films. *Nature materials*. 2016;15(3):304-10. doi:[10.1038/nmat4509](https://doi.org/10.1038/nmat4509)
66. Han S, Ciufu RA, Meyerson ML, Keitz BK, Mullins CB. Solvent-free vacuum growth of oriented HKUST-1 thin films. *Journal of Materials Chemistry A*. 2019;7(33):19396-406. doi:[10.1039/c9ta05179a](https://doi.org/10.1039/c9ta05179a)
67. Stassin T, Rodríguez-Hermida S, Schrode B, Cruz AJ, Carraro F, Kravchenko D, Ameloot R. Vapour-phase deposition of oriented copper dicarboxylate metal-organic framework thin films. *Chemical Communications*. 2019;55(68):10056-9. doi:[10.1039/c9cc05161a](https://doi.org/10.1039/c9cc05161a)
68. Cruz AJ, Stassen I, Krishtab M, Marcoen K, Stassin T, Rodríguez-Hermida S, Teyssandier J, Pletincx S, Verbeke R, Rubio-Giménez V. Integrated Cleanroom Process for the Vapor-Phase Deposition of Large-Area Zeolitic Imidazolate Framework Thin Films. *Chem Mater*. 2019;31:9462. doi:[10.1021/acs.chemmater.9b03435](https://doi.org/10.1021/acs.chemmater.9b03435)
69. Stassin T, Stassen I, Marreiros J, Cruz AJ, Verbeke R, Tu M, Reinsch H, Dickmann M, Egger W, Vankelecom IFJ. Solvent-Free Powder Synthesis and MOF-CVD Thin Films of the Large-Pore Metal-Organic Framework MAF-6. *Chem Mater*. 2020;32:1784. doi:[10.1021/acs.chemmater.9b03807](https://doi.org/10.1021/acs.chemmater.9b03807)
70. Stassin T, Stassen I, Wauteraerts N, Cruz AJ, Kräuter M, Coclite AM, de Vos D, Ameloot R. Solvent-Free Powder Synthesis and Thin Film Chemical Vapor Deposition of a Zinc Bipyridyl-Triazolate Framework. *Eur J Inorg Chem*. 2020;2020:71. doi:[10.1002/ejic.201901051](https://doi.org/10.1002/ejic.201901051)
71. Krishtab M, Stassen I, Stassin T, Cruz AJ, Okudur OO, Armini S, Wilson C, de Gendt S, Ameloot R. Vapor-deposited zeolitic imidazolate frameworks as gap-filling ultra-low-k dielectrics. *Nature Communications*. 2019;10:3729. doi:[10.1038/s41467-019-11703-x](https://doi.org/10.1038/s41467-019-11703-x)
72. Stassin T, Waitschat S, Heidenreich N, Reinsch H, Pluschkell F, Kravchenko D, Marreiros J, Stassen I, van Dinter J, Verbeke R. Aqueous Flow Reactor and Vapour-Assisted Synthesis of Aluminium Dicarboxylate Metal-Organic Frameworks with Tuneable Water Sorption Properties. *Chemistry*. 2020;26:10841. doi:[10.1002/chem.202001661](https://doi.org/10.1002/chem.202001661)
73. Tu M, Kravchenko DE, Xia B, Rubio-Giménez V, Wauteraerts N, Verbeke R, Vankelecom IFJ, Stassin T, Egger W, Dickmann M. Template-mediated control over polymorphism in the vapor-assisted formation of zeolitic imidazolate framework powders and films. *Angew Chem Int Ed*. 2021;133:7631. doi:[10.1002/anie.202014791](https://doi.org/10.1002/anie.202014791)
74. Stock N, Biswas S. Synthesis of metal-organic frameworks (MOFs): routes to various MOF topologies, morphologies, and composites. *Chemical reviews*. 2012;112(2):933-69. doi:[10.1021/cr200304e](https://doi.org/10.1021/cr200304e)
75. Mezenov YA, Kulachenkov NK, Yankin AN, Rzhavskiy SS, Alekseevskiy PV, Gilemkanova VD, Milichko VA. Polymer Matrix Incorporated with ZIF-8 for Application in Nonlinear Optics. *Nanomaterials*. 2020;10(6):1036. doi:[10.3390/nano10061036](https://doi.org/10.3390/nano10061036)
76. Isaeva VI, Kustov LM. Microwave activation as an alternative production of metal-organic frameworks. *Russian Chemical Bulletin*. 2016;65(9):2103-14. doi:[10.1007/s11172-016-1559-9](https://doi.org/10.1007/s11172-016-1559-9)
77. Thomas-Hillman I, Laybourn A, Dodds C, Kingman SW. Realising the environmental benefits of metal-organic frameworks: recent advances in microwave synthesis. *Journal of Materials Chemistry A*. 2018;6(25):11564-81. doi:[10.1039/c8ta02919a](https://doi.org/10.1039/c8ta02919a)
78. Khan NA, Jhung SH. Synthesis of metal-organic frameworks (MOFs) with microwave or ultrasound: Rapid reaction, phase-selectivity, and size reduction. *Coord Chem Rev*. 2015;285:11-23. doi:[10.1016/j.ccr.2014.10.008](https://doi.org/10.1016/j.ccr.2014.10.008)
79. Głowniak S, Szcześniak B, Choma J, Jaroniec M. Mechanochemistry: Toward green synthesis of metal-organic frameworks. *Materials Today*. 2021;46:109-24. doi:[10.1016/j.mattod.2021.01.008](https://doi.org/10.1016/j.mattod.2021.01.008)
80. Al-Kutubi H, Gascon J, Sudhölter EJR, Rassaei L. Electrosynthesis of Metal-Organic Frameworks: Challenges and Opportunities. *ChemElectroChem*. 2015;2(4):462-74. doi:[10.1002/celec.201402429](https://doi.org/10.1002/celec.201402429)
81. Liu J, Woll C. Surface-supported metal-organic framework thin films: Fabrication methods, applications, and challenges. *Chem Soc Rev*. 2017;46:5730-70. doi:[10.1039/C7CS00315C](https://doi.org/10.1039/C7CS00315C)

## Synthesis and research of polyfunctional silylureas used in electric deposition of tin-indium alloy

K.Yu. Ivanova , M.V. Kuzmin , L.G. Rogozhina , A.O. Patianova ,  
V.L. Semenov , R.I. Alexandrov 

Chuvash State University named after I. N. Ulyanov, 428015, Moskovskii pr., 15; Cheboksary, Russia

\* Corresponding author: [cool.karakyr@ya.ru](mailto:cool.karakyr@ya.ru)



This short communication (letter) belongs to the regular issue.

© 2021, The Authors. This article is published in open access form under the terms and conditions of the Creative Commons Attribution (CC BY) license (<http://creativecommons.org/licenses/by/4.0/>).

### Abstract

Polyfunctional silylureas were synthesized by the interaction of 3-aminopropyltriethoxysilane with isocyanates of various structures in an inert aromatic solvent. Commercially available diisocyanates such as isophorone diisocyanate, hexamethylene diisocyanate, 2,4-toluene diisocyanate were used as isocyanates. In this case, freshly distilled toluene was used as a solvent. The structures of the obtained compounds were confirmed by the data of IR and NMR<sup>1</sup>H spectroscopy. Using the synthesized compounds, formulations of compositions for electrodeposition of a tin-indium alloy on a copper wire were developed. The possibility of using silylureas of various structures as effective surfactants used in the electrodeposition of the tin-indium alloy is shown. The operational characteristics of the obtained wire were investigated, including the wire diameter, coating thickness, tensile strength, electrical resistance, and direct current electrical resistivity.

### Keywords

isophorone diisocyanate  
hexamethylene diisocyanate  
2,4-toluene diisocyanate  
3-aminopropyltriethoxysilane  
polyfunctional silylureas  
electrodeposition  
indium-tin alloy  
copper wire  
electrode  
solar panels

Received: 29.06.2021

Revised: 28.08.2021

Accepted: 31.08.2021

Available online: 13.09.2021

## 1. Introduction

One of the most important tasks of increasing the efficiency of photovoltaic solar modules is the search and development of new electrodes that provide high reliability of contact with crystalline silicon, as well as charge transfer in the cell [1]. Copper wire coated with various alloys, which is currently one of the main materials in electrical engineering, is widely used as conductive electrodes [2]. The use of such a wire ensures the reliability and protection of solar modules from any external influences and, as a result, the indicator of the durability of the product itself increases [3]. The use of a low-melting alloy on the surface of a copper wire makes it possible to obtain reliable electrical contact with a silver-containing contact grid, which helps to reduce the ohmic resistance between photovoltaic cells [4].

As a rule, wire coating is performed by electroplating or hot dipping [5]. The continuity of the contact of the electrode with monocrystalline silicon directly depends on the quality of the surface of the copper wire and the adhesion strength of the coating to the copper base, which ultimately affects the efficiency of transferring the convert-

ed light energy into electricity [6]. To obtain a microscopic adhesive layer of a copper wire coating, electrodeposition of a tin-indium alloy in various electrolytes can be used, but it is impossible to predict the effect of technological additives on the properties of the resulting coating; therefore, in most cases, the electrolyte composition is selected experimentally [6].

For the electrodeposition of the tin-indium alloy acidic and alkaline electrolytes are used. Of acidic electrolytes the following are used: perchlorate, sulfamic, chloride, glycerol, sulfate, boron fluoride electrolytes and others [7].

In the electrical and radio engineering industry, contact-reactive soldering with low-melting eutectic solders based on tin with indium and cadmium is widely used. Existing electrolytes based on Sn<sup>2+</sup> salts have low stability, even in the presence of special organic additives [8]. At the same time, there is information in the literature on the successful coprecipitation of tin with indium from acidic and alkaline electrolytes based on Sn<sup>4+</sup> salts [9], the stability of which is provided by oxyacids. The presence in the electrolyte of a hydroxy acid, for example citric acid, increases the content of the electronegative component of

the alloy [10, 11]. To develop a stable, reproducible and controlled technological process for obtaining eutectic composition solders from electrolytes based on  $\text{Sn}^{4+}$  salts, information is needed on the mechanism and kinetics of the joint discharge of alloy-forming metal ions.

The aim of the work was to increase the adhesion strength of the tin-indium alloy coating on a copper wire by using polyfunctional silylureas that meet the existing requirements for the production of electrodes for solar modules.

It is known that organosilicon compounds are surface-active, they can increase the intensity of biological processes of oxidation of organic pollution of wastewater and thereby reduce the anthropogenic load on the environment [12, 13].

## 2. Experimental

In this work, we synthesized organosilicon compounds - polyfunctional silylureas, which make it possible to increase the affinity of copper wire coated with a tin-indium alloy, improve the spreading of the solder, ensure the necessary activity of the composition, increase the contact angle with the surface during electrodeposition, reduce the surface tension and eliminate the oxidation of the solder surface and a base material to be electrodeposited.

Silylureas I-III received the interaction of 3-aminopropyltriethoxysilane with isocyanates of various structures in the presence of an antioxidant and toluene as a solvent at a temperature of 17-20 °C, while 2,4-toluene diisocyanate, hexamethylene diisocyanate, isophorone diisocyanate were used as isocyanates of various structures.

Fig. 1 shows a general scheme for the interaction of 3-aminopropyltriethoxysilane with diisocyanates. The data on yields, melting points and confirmation of the structures of polyfunctional silylureas are given in Table 1.

IR spectra were obtained on FT-801 series spectrophotometer in liquid paraffin.  $^1\text{H}$  NMR spectra were recorded

on a Bruker DRX500 spectrometer (500.13 MHz) in  $\text{DMSO-d}_6$ , the internal standard was tetramethylsilane. Mass spectra were recorded on a Finnigam MAT INCOS-50 instrument (ionizing electron energy 70 eV).

In the IR spectra of the obtained products, absorption bands are observed at 3309-3317, 1621-1632, 1562-1570  $\text{cm}^{-1}$ , characteristic of  $\text{NHC(O)NH}$  groups and at 1072-1074  $\text{cm}^{-1}$  Si-O bonds. In the  $^1\text{H}$  NMR spectra, there are characteristic signals belonging to the protons of the following groups ( $\delta$ , ppm): 0.50-0.56 t ( $\text{CH}_2\text{CH}_2\text{CH}_2\text{Si}$ ), 1.39-1.47 m ( $\text{CH}_2\text{CH}_2\text{CH}_2\text{Si}$ ) and at 2.94-3.04 m ( $\text{NHCH}_2\text{CH}_2\text{CH}_2\text{Si}$ ). The protons of the urea group correspond to signals at 6.52 t and 8.22 s for compound (I) and 5.69-5.71 t and 5.76-5.78 t, for compounds (II) and (III), respectively.

Silylureas are crystalline substances that melt without decomposition.

## 3. Results and discussion

At the next stage, tin-plated copper wires were obtained with the POIN-52 grade Sn-In alloy, which is used as a solder in electrical engineering. It is produced according to TU 48-0220-40-90. The wire thickness is 250  $\mu\text{m}$ , the coating thickness is from 3-5  $\mu\text{m}$ , which is applied by hot tinning.

Electrolyte formulations have been developed using synthesized polyfunctional silylureas. The container for electrolyte preparation was filled by three quarters with distilled water, and sulfuric acid was added to it in small portions. Then the solution was cooled to 20-22 °C, and the required amount of tin (II) sulfate was added to it and vigorously stirred to dissolve it. As-obtained solution was filtered. Then indium (III) sulfate was added to the filtrate and stirred until complete dissolution. Next, silylureas (I-III) (as surfactants to increase the affinity of the copper substrate with the alloy), previously dissolved in a small amount of isopropyl alcohol, were added to the solution,

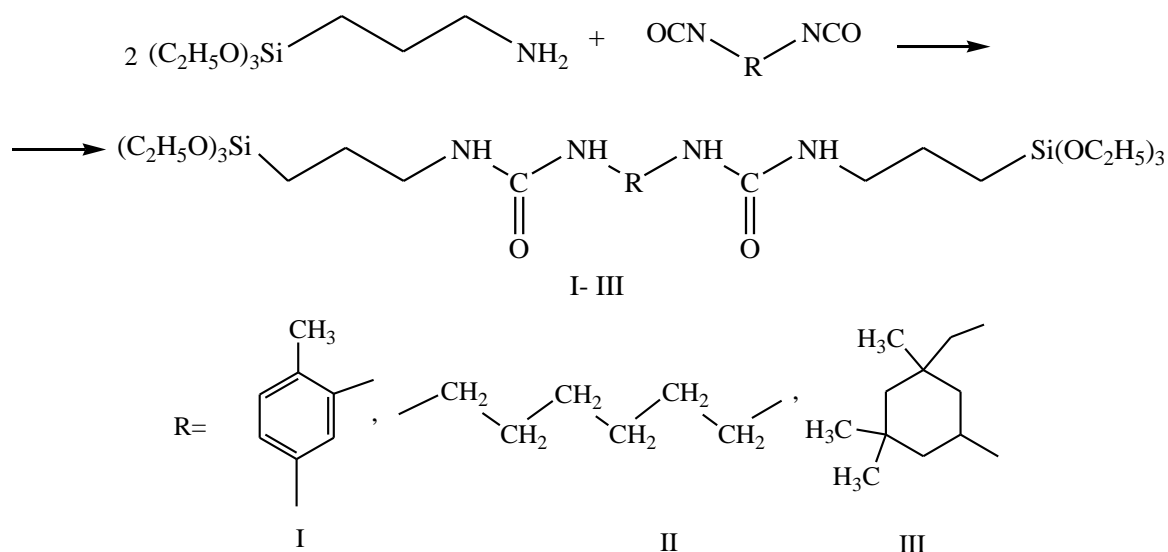


Fig. 1 Interaction of 3-aminopropyltriethoxysilane with diisocyanates

**Table 1** IR, NMR <sup>1</sup>H spectroscopy data and properties of polyfunctional silylureas

Name	Reaction yield, %	T <sub>m</sub> , °C	IR spectroscopy, cm <sup>-1</sup>	NMR spectroscopy, δ, ppm
2,4-toluylenebis[N-3-(triethoxysilyl)propyl]urea (I)	94.1	135	v 3309 (NH), δ 1632 (C=O <sub>amide I</sub> ), δ 1562 (NH <sub>amide II</sub> ), v 1072 (Si-O), v 1610 (ArH), δ 765 (ArH)	0.56 m (4H, 2CH <sub>2</sub> Si), 1.15 m (18H, 6 CH <sub>2</sub> CH <sub>2</sub> O, <sup>3</sup> J <sub>HH</sub> 7), 1.47 m (4H, 2CH <sub>2</sub> CH <sub>2</sub> CH <sub>2</sub> Si), 2.08 s (3H, CH <sub>3</sub> ), 3.04 m (4H, 2 NHCH <sub>2</sub> CH <sub>2</sub> CH <sub>2</sub> Si, <sup>3</sup> J <sub>HH</sub> 6.8), 3.75 m (12H, 6 CH <sub>2</sub> CH <sub>2</sub> O, <sup>3</sup> J <sub>HH</sub> 7), 6.52 t (2H, 2 NHC(O)NH C <sub>6</sub> H <sub>3</sub> , <sup>3</sup> J <sub>HH</sub> 5.6), 7.11 d, 7.45 d, 7.70 s (3H, C <sub>6</sub> H <sub>3</sub> ), 8.22 s (2H, 2 NHC(O)NH). M 616.89.
1,6-hexamethylenebis[N-3-(triethoxysilyl)propyl]urea (II)	95.9	122	v 3312 (NH), δ 1691 (C=O <sub>amide I</sub> ), δ 1570 (NH <sub>amide II</sub> ), v 1072 (Si-O)	0.50 t (4H, 2CH <sub>2</sub> Si, <sup>3</sup> J <sub>HH</sub> 8.45), 1.14 t (18H, 6 CH <sub>2</sub> CH <sub>2</sub> O, <sup>3</sup> J <sub>HH</sub> 7), 1.22 m (4H, 2CH <sub>2</sub> ), 1.33 m (4H, 2CH <sub>2</sub> ), 1.39 m (4H, 2CH <sub>2</sub> CH <sub>2</sub> CH <sub>2</sub> Si), 2.94 m (2 NHCH <sub>2</sub> CH <sub>2</sub> CH <sub>2</sub> Si, 2NHCH <sub>2</sub> , <sup>3</sup> J <sub>HH</sub> 6.8), 3.73 k (12H, 6CH <sub>2</sub> CH <sub>2</sub> O, <sup>3</sup> J <sub>HH</sub> 7), 5.71 t, 5.76 t (4H, 2NHC(O)NHCH <sub>2</sub> , <sup>3</sup> J <sub>HH</sub> 5.6). M 610.93.
isophoronbis[N-3-(triethoxysilyl)propyl]urea (III)	94.3	171	v 3317 (NH), δ 1624 (C=O <sub>amide I</sub> ), δ 1563 (NH <sub>amide II</sub> ), v 1070 (Si-O)	0.51 m (4H, 2CH <sub>2</sub> Si), 0.88-1.07 m (17H, 3 CH <sub>3</sub> , CH <sub>2</sub> , C <sub>6</sub> H <sub>6</sub> ), 1.14 t (18H, 6 CH <sub>2</sub> CH <sub>2</sub> O, <sup>3</sup> J <sub>HH</sub> 7), 1.39 m (4H, 2CH <sub>2</sub> CH <sub>2</sub> CH <sub>2</sub> Si), 2.94 m (4H, 2 NH CH <sub>2</sub> CH <sub>2</sub> CH <sub>2</sub> Si), 3.43 k (1H, CH <sub>cycle</sub> ), 3.74 k (12H, 6 CH <sub>2</sub> CH <sub>2</sub> O, <sup>3</sup> J <sub>HH</sub> 7), 5.69 t, 5.78 k (4H, 2 NHC(O)NH). M 636.97.

1,2-propylene glycol and the remaining amount of isopropyl alcohol were added to a predetermined level.

Co-deposition of Sn-In occurs electrochemically using the following deposition mode:

- Temperature, °C - 18-35;
- Cathode current density, A/dm<sup>2</sup> - 0.5-7.0;
- Current output, % - 80-98;
- The content of indium in the alloy, wt% - 40.0-52.0.

Measurement of the wire diameter, its deviation and ovality, the degree of alignment was carried out according to GOST 12177 using a video measuring system NVM-2010D. The determination of the thickness and composition of the coating was carried out in accordance with GOST 9.302 using an X-STRATA 920 X-ray fluorescence analyzer of coatings. The determination of the density was

carried out by hydrostatic weighing. Determination of tensile strength, yield strength, and relative elongation at breaking of the wire were carried out in accordance with GOST 10446 using an optical non-contact video extensometer M-VIEW and on a tensile testing machine RKM-1.1. The determination of the specific and electrical resistance was carried out according to GOST 7229. The adhesion strength of the adhesion of the coating of the tin-indium alloy with the copper base was studied by examining the coated wire after twisting with using the video measuring system NVM-2010D.

Tables 2 and 3 show the comparative characteristics of the developed electrolyte compositions, the properties of the electrolyte compositions of copper wire coated with a tin-indium alloy and the modes of its electrodeposition.

**Table 2** Electrolyte compositions for the production of copper wire coated with tin-indium alloy

Components, g / l	Compositions			
	Prototype	1	2	3
Tin sulphate (in terms of metal) (II)	2-15	17	17	17
Indium sulfate (in terms of metal) (III)	5-30	20	20	20
Sulfuric acid	90-100	80	85	80
Laureth 9	1-2	-	-	-
2,4-toluylenebis [N-3-(triethoxysilyl)propyl] urea (I)	-	1	-	-
1,6-hexamethylenebis [N-3-(triethoxysilyl)propyl] urea (II)	-	-	1	-
Isophoronbis [N-3-(triethoxysilyl)propyl] urea (III)	-	-	-	1
Isopropyl alcohol	-	10	10	10
Formalin (37% solution)	5-7	-	-	-
1,4-Butanediol (35% solution)	10-15	-	-	-
Propane-1,2-diol	-	20	25	15

**Table 3** Properties of coatings obtained by electrodeposition of a tin-indium alloy

Properties	Compositions			
	Prototype	1	2	3
Cathode current density, A/dm <sup>2</sup>	0.5-7.0	20.0	20.0	20.0
Temperature, °C	15-30	18	18	18
Alloy current output, %	37-97	87	85	80
Indium content in the alloy, %	0.5-56.0	41.0	42.0	40.0
Appearance of coatings	shiny	smooth shiny surface and continuous coating along the entire length of the wire		
Leveling degree	0.20-0.60	0.85	0.80	0.80
Adhesive strength test	-	+	+	+
Wire diameter, μm	-	250	250	250
Coating thickness, microns	6	0.1	0.1	0.1
Coating density, g / cm <sup>3</sup>	-	8.9	8.9	8.9
Tensile strength of wire, N/ mm <sup>2</sup>	-	242	238	240
Relative extension, %	-	23	24	21
DC electrical resistance at 20 °C, Ohm / m	-	0.35	0.35	0.35
Specific electrical resistance for direct current at a temperature of 20 °C, Ohm mm <sup>2</sup> / m	-	0.0172	0.0174	0.0176

As can be seen from Tables 2 and 3, the copper wires obtained by this method with a coating based on a tin-indium alloy from the proposed electrolyte have a smooth shiny surface and a continuous coating with a thickness of 0.1 – 1.0 μm along the entire length of the wire, strong adhesion to a copper base and the presented modes of electrodeposition can be used to obtain a microscopic adhesive layer of a copper wire coating based on a tin-indium alloy.

#### 4. Conclusions

Polyfunctional silylureas were synthesized via the interaction of 3-aminopropyltriethoxysilane with isocyanates of various structures, which were used as active surfactants in the electrodeposition of a tin-indium alloy. The qualitative and quantitative composition of the electrolyte for the electrodeposition of the tin-indium alloy on copper wire and the production of electrodes for solar modules was selected based on the use of effective modifiers that increase the adhesive strength of the coating on a copper substrate. It was found that the synthesized polyfunctional silylureas increase the affinity of copper wire coated with a tin-indium alloy and, consequently, the binding power and adhesive strength. The use of the developed electrolyte with the polyfunctional silylureas in the electrodeposition of a tin-indium alloy on a copper wire makes it possible to obtain an electrode for solar panels with high physical, mechanical and operational properties.

#### Acknowledgments


The research was carried out in Chuvash state University within the implementation of a comprehensive project under the contract No. 2019/0837/1202–19 dated September 19, 2019 with the financial support of the Ministry of Education and Science of Russia under the Agreement No. 075-11-2019-047 dated November 25, 2019 and Russian Foundation for Basic Research (RFBR), project number 20-33-90269.

#### References

1. Prospects for Energy Technologies 2008. Scenarios and Strategies until 2050 [Internet]. International Energy Agency. OECD / IEA, 2008. p. 10-15 [cited 29.07.2021]. Available from: <https://iea.blob.core.windows.net/assets/0e190efb-daec-4116-9ff7-ea097f649a77/etp2008.pdf>
2. Lobanov ML, Kardonina NI, Rossina NG, Yurovskikh AS. Zashchitnye pokrytiya : uchebnoe posobie [Protective coatings: textbook]. Yekaterinburg: Ural Federal University Publishing House; 2014. p. 87-89. Russian.
3. Vinokurov EG, Margolin LN, Farafonov VV. Elektroosazhdenie kompozitsionnykh pokrytiy [Electrodeposition of composite coatings]. Izvestiya vysshikh uchebnykh zavedeniy. Seriya: Khimiya i khimicheskaya tekhnologiya., 2020;63(8):4-38. Russian.
4. Bessel VV, Kucherov VG, Mingaleeva RD. Izuchenie solnechnykh fotoelektricheskikh elementov [Study of solar photovoltaic cells]. Moscow: Publishing Center of the Russian State University of Oil and Gas (NRU), 2016. p. 36-37. Russian.
5. Toshio I, Yuichi M, Toshihide U, Hajime K, Susumu Y, Masayuki T. Electrochemical deposition of a Ni - fluoroplastic composite film on the powder of a hydrogen-absorbing AB5 type alloy. Nippon kagaku kaishi. 2001;7:387-391.

6. Zorkina OV, Perelygin YuP. Elektroosazhdeniye splava olovo-indiy iz sulfatnogo elektrolita [Electrodeposition of a tin - indium alloy from a sulfate electrolyte]. Materialy Vserossiyskoy konferentsii «Progressivnaya tekhnologiya i voprosy ekologii v galvanotekhnike i proizvodstve pechatnykh plat» [Book of abstracts of “Progressive technology and environmental issues in electroplating and printed circuit board production” conference]. Penza: DNTP, 2000. p. 48-49. Russian.
7. Fursova NYu. Elektroosazhdeniye splava Sn-Sb iz sulfata elektrolity s organicheskimi dobavkami [Electrodeposition of Sn-Sb alloy from sulfate electrolytes with organic additives] [dissertation]. Moscow: Mendeleev University of Chemical Technology, 2000. 146 p. Russian.
8. Kryvtsov AK, Khamaev VA, Gryaznova GI, Pavelyeva LA, Karabinov YuV, inventors. Elektrolit dlya osazhdeniya pokrytiy iz splava olovo-indiy. USSR patent SU 865997 A1. 23 Sep 1981. Russian.
9. Perelygin YuP. Elektroosazhdeniye indiya i splavov na ego sonove. Raspredeleniye toka mezhdou sovmestnymi reaktsiyami vosstanovleniya ionov na katode [Plating indium and its alloys. Current distribution between joint recovery reactions of ions reduction at the cathode] [dissertation]. Moscow: Mendeleev University of Chemical Technology. 1996. 235 p. Russian.
10. Kotov VL, Gryaznova GI, Chuvilyaeva TV, Kryvtsov AK. Izvestiya Vysshikh Uchebnykh Zavedeniy Seriya “Kimiya i Khimicheskaya Tekhnologiya”. 1985;28(9):70-73. Russian.
11. Belevskiy SS. Indutsirovannoe soosazhdenie nanokristallicheskikh Co-W pokrytiy I ikh mekhanicheskie svoystva [Induced coprecipitating of nano-crystalline Co-W coatings and their mechanical properties] [dissertation]. Chisinau: Institute of Applied Physics; 2012. 142 p. Russian.
12. Patianova AO, Ivanova KYu, Rogozhina LG, Kuzmin MV, Semenov VL. Improving the environmental production of electrodes for solar panels. Chimica Techno Acta. 2020;7(4):186-191. doi:[10.15826/chimtech.2020.7.4.09](https://doi.org/10.15826/chimtech.2020.7.4.09)
13. Ivanova KYu, Kuzmin MV, Kol'tsov NI. Synthesis and research of polyfunctional siliconcontaining amines - new promoters of adhesion. Chimica Techno Acta. 2020;7(4):199-203. doi:[10.15826/chimtech.2020.7.4.11](https://doi.org/10.15826/chimtech.2020.7.4.11)

## Effect of Al<sub>2</sub>O<sub>3</sub> and CaF<sub>2</sub> additives on the viscosity of conventional cryolite melts

A.S. Lyutina<sup>ab</sup>, A.A. Kataev<sup>b</sup>, A.V. Rudenko<sup>b</sup>, O.Yu. Tkacheva<sup>ab\*</sup> 

a: Ural Federal University, 19 Mira St., Yekaterinburg 620002, Russia

b: Institute of High-Temperature Electrochemistry Ural Branch of the Russian Academy of Sciences, 20 Akademicheskaya St., Yekaterinburg 620137, Russia

\* Corresponding author: [o.tkacheva@ihte.uran.ru](mailto:o.tkacheva@ihte.uran.ru)



This article belongs to the regular issue.

© 2021, The Authors. This article is published in open access form under the terms and conditions of the Creative Commons Attribution (CC BY) license (<http://creativecommons.org/licenses/by/4.0/>).

### Abstract

The viscosity of cryolite melts of conventional composition NaF–AlF<sub>3</sub>–CaF<sub>2</sub>–Al<sub>2</sub>O<sub>3</sub> was studied by rotational viscometry using the FRS 1600 high-temperature rheometer. The cryolite ratio of the NaF–AlF<sub>3</sub> melt was 2.1, 2.3, and 2.5; the Al<sub>2</sub>O<sub>3</sub> content varied from 2 to 6.6, and CaF<sub>2</sub> – from 0 to 8 wt%. The measurements were carried out in the temperature range from liquidus to 1200 °C. The conditions for the laminar flow of the investigated melts were determined, based on the measurements of the cryolite melts viscosity as a function of the shear rate at a constant temperature. A shear rate of  $12 \pm 1 \text{ s}^{-1}$  was chosen for studying the viscosity temperature dependence for all samples. The viscosity temperature dependence of cryolite melts is described by a linear equation. The temperature coefficient *b* in this equation has negative values and varies in the range of (–0.01)–(–0.06) mPa·s/deg. It was found that the viscosity of cryolite melts of conventional composition in the range of operating temperatures of aluminum electrolysis (950–970 °C) varies from 2.5 to 3.7 mPa·s (depending on the composition and temperature). The viscosity of cryolite-alumina melts increases with the rise of alumina content: 1 wt% Al<sub>2</sub>O<sub>3</sub> increases the viscosity, on average, by 1%. However, the influence of CaF<sub>2</sub> is more significant: the addition of 1 wt% CaF<sub>2</sub> leads to an increase in viscosity by 3%. A decrease in the CR of the melt by 0.1 (in the range of 2.1–2.5) leads to a decrease in the viscosity of cryolite melts by 2.3%. A viscosity regression equation for the cryolite melts of conventional composition as a function of several independent parameters (temperature, CR, CaF<sub>2</sub> and Al<sub>2</sub>O<sub>3</sub> content) is obtained by the multivariable approximation of experimental data. The equation satisfactorily (within 1.5%) describes the viscosity of conventional industrial electrolytes and can be used for estimation of their viscosity.

### Keywords

molten cryolite  
alumina  
calcium fluoride  
viscosity  
rotary method

Received: 02.07.2021

Revised: 16.08.2021

Accepted: 13.09.2021

Available online: 21.09.2021

### 1. Introduction

According to the International Aluminum Institute, the worldwide aluminum production amounted 65.296 million tons in 2020, of which 3.72 million tons were produced in Russia. Nonetheless, the classic Hall–Héroult process for producing aluminum is more than 140 years old. It is comprised on the electrolysis of dissolved aluminum oxide (alumina) in molten cryolite. The melting point of alumina is 2044 °C, therefore, in order to obtain primary alumi-

num, the alumina has to be dissolved in sodium cryolite, whereas electrolysis is carried out at 950–970 °C.

The conventional electrolyte is composed on the base of sodium cryolite (Na<sub>3</sub>AlF<sub>6</sub>), besides the additions of AlF<sub>3</sub>, CaF<sub>2</sub>, MgF<sub>2</sub> are added [1]. These electrolytes possess a high solubility of alumina [2]. The electrolyte is characterized by such parameter as the cryolite ratio (CR), expressed by the molar ratio of sodium fluoride to aluminum fluoride. The sodium cryolite has the CR = 3, and the CR of industrial electrolytes can vary from 2.1 to 2.7 [3].

One of the main parameters defining the electrolysis process is the current efficiency. The current efficiency during electrolysis is influenced by many factors: process temperature, pole-to-pole distance, current density, composition and physicochemical properties of the electrolyte, cell design, etc. One of the most important characteristics of molten cryolite-alumina electrolytes, which determine the processes of mass and heat transfer in an aluminum cell, is viscosity. It also determines the following hydrodynamic processes: electrolyte circulation, rate of alumina dissolution, flotation and sedimentation of alumina particles, transfer of dissolved and undissolved alumina in the electrolyte bulk, transfer and release of anode gas, nature of chemical and electrode reactions [4, 5].

Nowadays, the most reliable and systematic data related to the viscosity of cryolite melts is considered to be the results obtained by Torklep and Oye in 1980 [6]. They measured the viscosity of cryolite melts in wide ranges of CR (the  $\text{AlF}_3$  content was varied from 5 to 35 mol.%) and temperature by an oscillation method. The viscosity of cryolite melts depending on CR was obtained to be non-linear. The maximum value ( $\sim 2.3$  mPa/s at 1000 °C) accumulated in the melt with CR = 4. Abnormal behavior of melts with low CR was detected (random movements of the pendulum, very large differences between periodic viscosity and damping viscosity, irreproducibility of results, etc.). The authors suggest that one of the several possible reasons for the observed behavior of acidic melts is insufficient mixing. In the region of high CRs, the difficulties in dissolving of oxide were noted. It was the reason for the increase in the duration of experiments in order to obtain completely reproducible values. The viscosity measurements were carried out from high temperature in every 10–20 degrees, lowering temperature to the expected liquidus point. The frequent overcooling of the cryolite-alumina melts was observed, which led to the fact that measurements of some compositions were conducted in the two-phase region. In cryolite-alumina melts with the  $\text{Al}_2\text{O}_3$  content up to 4 wt%, the viscosity temperature dependences were almost parallel to the curves obtained in the NaF– $\text{AlF}_3$  binary system, especially for melts with low CR. The inflection point on the binary curve become even more pronounced with an increase in the  $\text{Al}_2\text{O}_3$  content.

Authors [6, 7, 8] measured the viscosity of the NaF– $\text{AlF}_3$ – $\text{Al}_2\text{O}_3$  ternary system depending on CR and  $\text{Al}_2\text{O}_3$  concentration. It should be noted that some experimental results were presented at temperatures below the liquidus of the corresponding mixtures. This may explain why the measured viscosities of these two-phase samples (consisting of a suspension of some solid particles of aluminum oxide and corundum in the liquid phase) are significantly higher than the calculated viscosities of "hypothetical" liquid (single-phase) samples. In this case, no bends are observed on the curves.

The viscosity of cryolite melts containing  $\text{CaF}_2$  were described in articles [8, 9]. The viscosity values obtained by different authors differ significantly. Moreover, the comparison of viscosity values is often difficult due to the significantly different multicomponent mixtures of cryolite melts.

Researchers [5] determined the temperature dependences of density, viscosity, surface and interfacial tension in a system with low CR: 55 mol.% NaF + 45 mol.%  $\text{AlF}_3$ . The viscosity was measured in the temperature range from 725 to 840 °C, and a quadratic equation for the viscosity temperature dependence was obtained for the cryolite melts of eutectic composition (CR = 1.22).

In paper [10] a thermodynamic model was suggested for calculating the viscosity of multicomponent fluoride systems. The authors used the thermochemical program FactSage [11].

Thus, despite the importance of viscosity for the technological process, the viscosity of cryolite melts of conventional electrolytes has not been properly studied yet. According to various authors, the viscosity of the conventional electrolyte NaF– $\text{AlF}_3$ – $\text{CaF}_2$ – $\text{Al}_2\text{O}_3$  in the CR range from 1.8 to 2.6 and 945–970 °C varies in the range from 1 to 5 mPa·s [10, 12].

The limited number of studies related to the viscosity of cryolite melts can be explained by the great experimental difficulties associated with the choice of structural materials, due to the aggressiveness of fluoride melts and high measurement temperatures (about 1000 °C), as well as with rather low values of the molten salts viscosity.

The purpose of this work was to study the effect of temperature, cryolite ratio,  $\text{CaF}_2$  and  $\text{Al}_2\text{O}_3$  content on the viscosity of cryolite melts of the conventional composition NaF– $\text{AlF}_3$ – $\text{CaF}_2$ – $\text{Al}_2\text{O}_3$  with the CR = 2.1–2.5 in a wide temperature range using the rotational viscometry; the focus was also set on the obtaining of the viscosity multiparameter regression equation for the molten conventional electrolytes.

## 2. Experimental

### 2.1. Composition and preparation of melts

Molten mixtures were prepared from individual substances NaF (specifically pure grade),  $\text{AlF}_3$  (highly pure grade), and  $\text{CaF}_2$  (pure grade) (Vekton).

A weighed amount of components was loaded into a glassy carbon crucible and remelted at 990 °C for 2 hours in a shaft furnace. The prepared mixtures were stored in a closed container.

The compositions of the studied samples are presented in Table 1.

### 2.2. Rotational viscometry method

A liquid is placed in a small gap, necessary for the shear of the medium, between two cylinders: an inner cylinder with a radius  $R_o$  and an outer one with a radius  $R_i$ .

**Table 1** Composition of cryolite melts

CR	NaF		AlF <sub>3</sub>		CaF <sub>2</sub> , wt%	Al <sub>2</sub> O <sub>3</sub> , wt%
	wt%	mol.%	wt%	mol.%		
2.1	48.7	65.3	46.3	31.1	0	3.0
					5.0	3.0
					5.0	6.5
					8.0	6.5
2.3	50.8	67.2	44.2	29.2	0	2.0
					5.0	2.0
					5.0	4.0
					0	2.0
2.5	52.8	68.9	42.2	27.6	5.0	2.0
					5.0	4.0
					5.0	6.0
					5.0	6.0

A schematic diagram of a rotating cylindrical viscometer is shown in Fig. 1.

During measurements, the outer cylinder rotates at a constant rate, while the inner cylinder is given a rotational torque, which is a measure of viscosity. The viscosity ( $\eta$ ) is calculated by the following equation:

$$\eta = \frac{1}{\omega} \left( \frac{M}{4\pi h} \right) \left( \frac{1}{R_i^2} - \frac{1}{R_o^2} \right) = k \frac{M}{\omega} \tag{1}$$

where  $M$  is the torque acting on the cylindrical surface, N·m;  $\omega$  is the angular velocity, rad/s;  $h$  is the depth of immersion of the inner cylinder in a liquid medium, m;  $R_i$  is the radius of the inner cylinder, m;  $R_o$  is the radius of the outer cylinder, m;  $k$  - is the constant of the device, rad/m<sup>3</sup>.

The parallel plane model, schematically depicted in Fig. 2, helps defining both shear stress ( $\tau$ ) and shear rate ( $\dot{\gamma}$ ) [13].

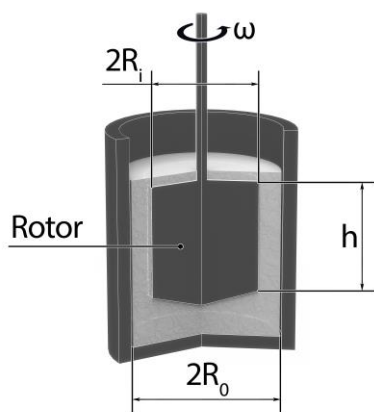


**Fig. 1** Schematic diagram of a cylindrical viscometer

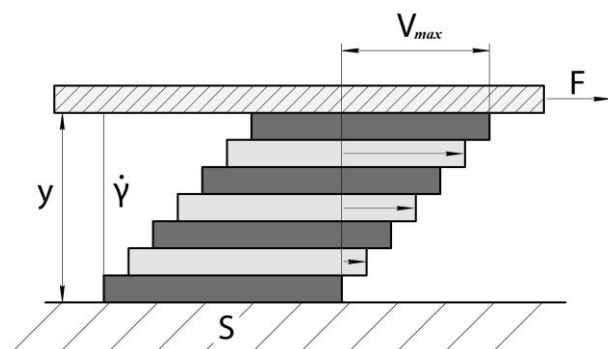


**Fig. 2** The flow between two parallel planes

The force  $F$ , applied to the area  $S$  located at the interface between the upper plane and the fluid below it, causes a flow in the fluid layer:

$$\tau = \frac{F}{S} \tag{2}$$

where  $\tau$  is the shear stress, Pa (N/m<sup>2</sup>);  $F$  is the force applied to the area  $S$ , N;  $S$  is the area, m<sup>2</sup>.

The shear stress produces a characteristic pattern of layer-by-layer rate distribution in the fluid layer. The maximum flow rate  $V_{max}$  is observed at the interface between the liquid and the moving plane [13].

The flow rate decreases with the distance from the moving plane, and at a distance  $y$  from it, at the boundary with the fixed plane,  $V_{min} = 0$ . The laminar flow means that the liquid layers of infinitesimal thickness slide over one another. One laminar layer is displaced relative to the other by some part of the total shear of the entire liquid layer between both planes. The velocity gradient across the gap is called the shear rate, which is mathematically expressed as a differential:

$$\dot{\gamma} = \frac{dv}{dy}, \quad \left[ \frac{\text{m/s}}{\text{m}} = \text{s}^{-1} \right]. \tag{3}$$

The dynamic viscosity is defined as

$$\eta = \frac{\tau}{\dot{\gamma}}, \quad \left[ \frac{\text{N/m}^2}{\text{s}^{-1}} = \text{Pa} \cdot \text{s} \right]. \tag{4}$$

### 2.3. Measurement techniques

The viscosity measurements of the cryolite melts with different CR and additive concentrations were carried out using an FRS 1600 rheometer, the principle of operation of which is based on the rotary method.

The studied sample is placed in an outer graphite cylinder (Fig. 3). The inner cylinder slowly immerses and rests against the solid sample with a force of 3 N, after which the furnace starts heating. After reaching the liquidus temperature, the rotor begins rotating at a low rate in order to homogenize the melt. The fact that the sample has passed into a single-phase state can be judged by the steady-state values of the viscosity. The viscosity measurements can be performed either at a constant temperature or according to a given program for cooling the melt in a dynamic mode.

## 3. Results and discussion

### 3.1. Selecting the "shear rate" parameter

In order to obtain the correct viscosity values, a laminar flow has to be established in the sample. This means that it takes time for the substance to start moving at a rate corresponding to the applied shear stress.

In order to determine the conditions for the laminar flow the viscosity of all cryolite samples was measured as a function of the shear rate at a constant temperature. As

an example, the dependence of the viscosity of cryolite samples with the CR = 2.5 on the shear rate in logarithmic coordinates is presented in Fig 4. The shear rate varies from 2 to 50 s<sup>-1</sup>.

It is seen in the Fig. 4 that at low shear rate (up to 10 s<sup>-1</sup>), a large scatter of points is observed, which is due to the fact that the laminar flow was not established yet. The laminar flow is realized when the viscosity does not depend on the shear rate, that is, in the horizontal section in the shear rate range of 10–16 s<sup>-1</sup>. With an increase in the shear rate above 16 s<sup>-1</sup>, the viscosity rises sharply, which is associated with incipient turbulence.

In order to study the temperature dependence of the viscosity of all samples, a shear rate of 12 ± 1 s<sup>-1</sup> was chosen.

### 3.2. The viscosity temperature dependence of the cryolite melts

The viscosity measurements were started at 1020 °C, then the temperature was decreased to a temperature few degrees above liquidus. The cooling rate was 2 °C/ min. The liquidus temperature was calculated using the equation given in [14]. The calculated values of the liquidus temperature are listed in Table 2.

The viscosity temperature dependence of the cryolite melts with the CR = 2.1 is given in Fig. 5.

The viscosity temperature dependence of all samples in the temperature range from the liquidus to 1200 °C is described by a linear equation of the type:

$$\eta = a + bT \quad (5)$$

where  $a$  and  $b$  are experimental constants.

The equations for the viscosity temperature dependence of the cryolite melts are summarized in Table 2. For all equations, the coefficient of determination  $R^2$  has a value of at least 0.97. The viscosity of the cryolite samples at the operating temperatures of aluminum electrolysis 950 and 970 °C are given in Table 2.

As the temperature rises the viscosity of the molten salt decreases.



Fig. 3 Internal and external cylinders and the shaft furnace Carbolite STF16/180

The temperature coefficient  $b$  in equation (5) has negative values and varies in the range of (–0.01)–(–0.06) mPa·s/deg for all tested samples. Thus, the change in temperature has a decisive influence on the change in the viscosity of the electrolyte.

### 3.3. Effect of CR, CaF<sub>2</sub> and Al<sub>2</sub>O<sub>3</sub> content

The viscosity temperature dependence of the cryolite-alumina melts with different CR is shown in Fig. 6. The figure also demonstrates the literature data [6] and [15] on the viscosity of melts, which are the closest to ours in composition and temperature range of measurements.

The data diverge quite significantly, although the temperature coefficients are close. It should be noted that due to the complex multicomponent compositions of electrolytes for aluminum production, it is difficult to find completely identical compositions in the references, and no generalizing equations have been found. Moreover, the results of works [6] and [15] were obtained by the oscillation method, the disadvantages of which were described above. In addition, data on the density were used to calculate the dynamic viscosity of these compositions, which introduces an additional error in the result.

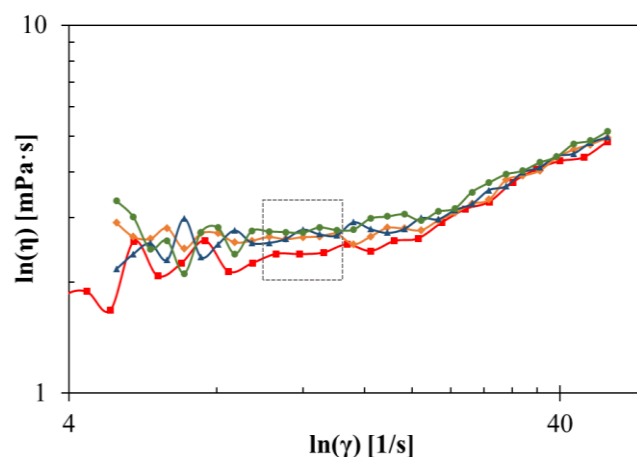


Fig. 4 The viscosity of cryolite melts with the CR = 2.5 depending on the shear rate at 1020 °C: ■ – without additives; ◆ – 5 wt% CaF<sub>2</sub>; ▲ – 5 wt% CaF<sub>2</sub> and 2 wt% Al<sub>2</sub>O<sub>3</sub>; ● – 5 wt% CaF<sub>2</sub> and 2 wt% Al<sub>2</sub>O<sub>3</sub>

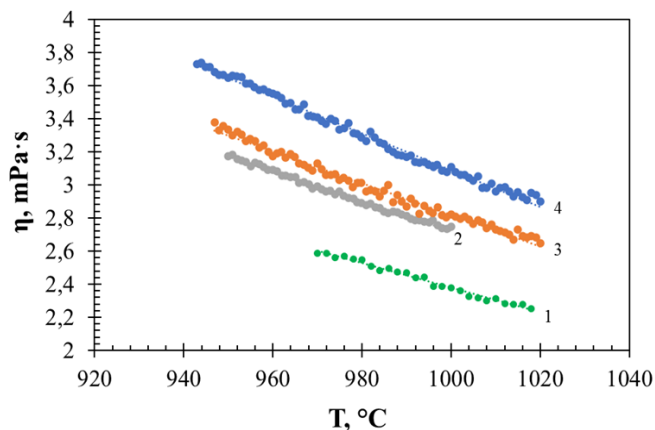


Fig. 5 The viscosity temperature dependence of the cryolite melts with CR = 2.1 and different content of CaF<sub>2</sub> and Al<sub>2</sub>O<sub>3</sub> (wt%): 1 – 0 CaF<sub>2</sub> + 3 Al<sub>2</sub>O<sub>3</sub>; 2 – 5 CaF<sub>2</sub> + 3 Al<sub>2</sub>O<sub>3</sub>; 3 – 5 CaF<sub>2</sub> + 6.5 Al<sub>2</sub>O<sub>3</sub>; 4 – 8 CaF<sub>2</sub> + 6.5 Al<sub>2</sub>O<sub>3</sub>

**Table 2** Viscosity (mPa·s) of the cryolite melts of conventional composition

Nº	CR	CaF <sub>2</sub> , wt%	Al <sub>2</sub> O <sub>3</sub> , wt%	<i>a</i>	<i>b</i>	<i>R</i> <sup>2</sup>	<i>η</i> (950 °C)	<i>η</i> (970 °C)	<i>T</i> <sub>liq</sub> [14]
1		0	3.0	9.837	-0.0075	0.985	-	2.56	958
2	2.1	5.0	3.0	11.716	-0.009	0.99	3.17	2.99	940
3		5.0	6.5	12.37	-0.0096	0.98	3.25	3.06	931
4		8.0	6.5	14.234	-0.0111	0.99	3.67	3.46	920
5		0	2.0	10.023	-0.0075	0.97	-	2.67 (980 °C)	975
6	2.3	5.0	2.0	9.011	-0.0063	0.97	-	2.90	960
7		5.0	4.0	9.832	-0.007	0.98	3.18	3.04	949
8		0	2.0	9.506	-0.0069	0.75	-	-	990
9		5.0	2.0	9.9867	-0.0072	0.93	-	-	978
10	2.5	5.0	4.0	10.168	-0.0073	0.96	-	2.97 (980 °C)	965
11		5.0	6.0	10.438	-0.0075	0.97	-	3.115	958

According to our data, the CR alteration by 0.1 changes the viscosity of cryolite-alumina melts in average by 0.1 mPa·s, which is 2.3%. The viscosity of cryolite melts in the temperature range of 950-970 °C varies from 2.5 to 3.7 mPa·s (depending on the composition).

It can be concluded, based on the results presented in Table 2, that both the CaF<sub>2</sub> and Al<sub>2</sub>O<sub>3</sub> additives effect the cryolite melts viscosity.

The viscosity of cryolite-alumina melts rises with increasing alumina content. The addition of 1 wt% Al<sub>2</sub>O<sub>3</sub> increases by 1% the viscosity of conventional electrolyte, on average.

Calcium fluoride significantly increases the viscosity of cryolite-alumina melts. The addition of 1 wt% CaF<sub>2</sub>, on average, increases the electrolyte viscosity by 3%. Considering that CaF<sub>2</sub> impacts the thermal conductivity of cryolite melts, and acts as a part of the side ledge of the electrolysis bath, that is, plays an important role in the thermal balance of an aluminum cell, its concentration in conventional electrolyte is an important value and requires special control.

### 3.4. Multiparameter equation of the viscosity

The general regression equation for the dependence of the conventional cryolite electrolyte viscosity on several parameters was derived by the multivariable data approximation. The data set included the following parameters: temperature, cryolite ratio, calcium fluoride and alumina content. The resulting equation for the viscosity of cryolite melts is the following:

$$\eta = 71.75 - 0.133 \cdot T - 8.21 \cdot 10^{-3} \cdot C(\text{Al}_2\text{O}_3) + 0.333 \cdot CR + 0.0796 \cdot C(\text{CaF}_2) - 0.625 \cdot 10^{-5} \cdot T^2 - 2.08 \cdot \left( \frac{C(\text{CaF}_2) + C(\text{Al}_2\text{O}_3)}{C(\text{Al}_2\text{O}_3)} \right)^{1.5} + 8.12 \cdot 10^{-5} \cdot C(\text{Al}_2\text{O}_3)^3; \quad (6)$$

$R^2 = 0.99$

where *T* is temperature, °C; *C*(Al<sub>2</sub>O<sub>3</sub>) and *C*(CaF<sub>2</sub>) are the content of components, wt%; CR is the cryolite ratio.

The equation is valid within the temperature range from liquidus to 1020 °C at CR 2.1-2.5, the CaF<sub>2</sub> content 0-8 wt%, the Al<sub>2</sub>O<sub>3</sub> content 2-6.5 wt%.

The equation is valid in the temperature range from liquidus temperature to 1020 °C, in the concentration ranges of CR 2.1-2.5, alumina from 2 to 6.5 wt%, and calcium fluoride from 0 to 8 wt%.

A comparison of the experimental and calculated by equation (6) viscosity data for the cryolite melt with CR = 2.3 is shown in Fig. 7.

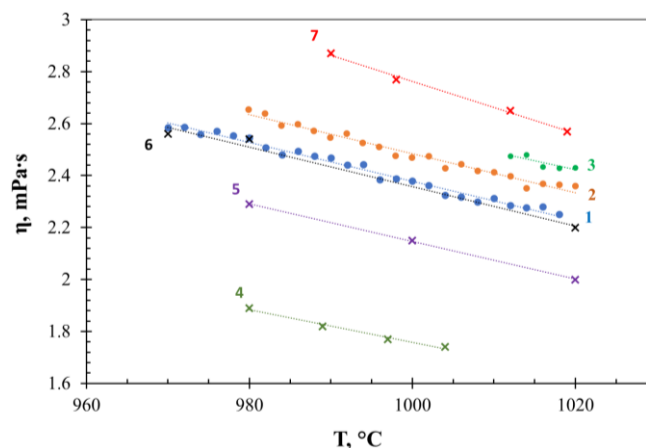


**Fig. 6** The viscosity temperature dependence of the NaF-AlF<sub>3</sub> melt with different CR and Al<sub>2</sub>O<sub>3</sub> content (wt%): 1 - CR = 2.1, Al<sub>2</sub>O<sub>3</sub> = 3; 2 - CR = 2.3, Al<sub>2</sub>O<sub>3</sub> = 4; 3 - CR = 2.5, Al<sub>2</sub>O<sub>3</sub> = 2; 4 - CR = 2.1 [15]; 5 - CR = 2.3, Al<sub>2</sub>O<sub>3</sub> = 4 [6]; 6 - CR = 2.3, Al<sub>2</sub>O<sub>3</sub> = 8 [6]; 7 - CR = 2.3, Al<sub>2</sub>O<sub>3</sub> = 12 [6]

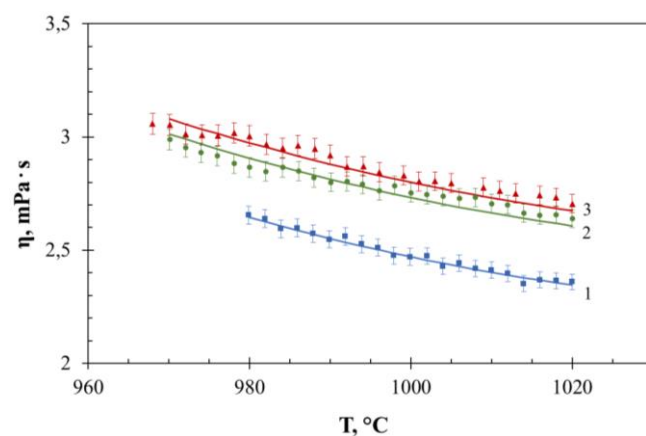


**Fig. 7** Experimental and calculated viscosity for cryolite melts with CR = 2.3. Concentration of additives - in wt%: 1 - CaF<sub>2</sub> = 0, Al<sub>2</sub>O<sub>3</sub> = 2; 2 - CaF<sub>2</sub> = 5, Al<sub>2</sub>O<sub>3</sub> = 2; 3 - CaF<sub>2</sub> = 5, Al<sub>2</sub>O<sub>3</sub> = 4; points - experiment, lines - calculation

The calculated viscosity is given as solid lines in Fig. 4 and the experimental data – as dots. The experimental and calculated values of the viscosity of conventional cryolite electrolyte coincide within 1.5%.

## Conclusions

The viscosity of the conventional cryolite melts NaF–AlF<sub>3</sub>–CaF<sub>2</sub>–Al<sub>2</sub>O<sub>3</sub> in the temperature range of 950–970 °C varies from 2.5 to 3.7 mPa·s (depending on the composition). The viscosity increases with the rise in the content of additives: per addition of 1 wt% Al<sub>2</sub>O<sub>3</sub> the viscosity, on average, increases by 1%, while the addition of 1 wt% CaF<sub>2</sub> increases the melt viscosity by 3%. A decrease in the CR of the melt by 0.1 results in a viscosity decrease (in the range of the CR 2.1–2.5) by 2.3%.

The regression equation for estimating viscosity of cryolite melts on several independent parameters, obtained by approximating the experimental data, satisfactorily describes (within 1.5%) the viscosity of conventional electrolytes for aluminum production.

## References

1. Kudryavtseva NT. Prikladnaya electrokimiya [Applied electrochemistry]. Moscow: Khimiya; 1975. 552 p. Russian.
2. Grjotheim K, Krohn C, Malinovsky M, Matiasovsky K, Thonstad J. Aluminium electrolysis. Fundamentals of the Hall-Heroult process. 2nd ed. Dusseldorf: Aluminium-Verlag; 1982. 443 p.
3. Borisoglebskiy YuV, Galevskiy GV, Kulagin NM. Metallurgiya alyuminia [Metallurgy of aluminum]. Novosibirsk: Nauka; 1999. 438 p. Russian.
4. Haupin W. The influence of additives on Hall-Heroult bath properties. JOM. 1991;43:28–34.
5. Silny A, Chrenkova M, Danek V. Density, viscosity, surface tension, and interfacial tension in the systems NaF(KF) + AlF<sub>3</sub>. J Chem Eng Data. 2004;49:1542–1545. doi:[10.1021/jeo341965](https://doi.org/10.1021/jeo341965)
6. Torklep K, Oye H. Viscosity of NaF–AlF<sub>3</sub>–Al<sub>2</sub>O<sub>3</sub> melt mixtures. Electrochimica Acta. 1980;25:229–235.
7. Hertzberg T, Torklep K, Oye H. Viscosity of NaF–AlF<sub>3</sub>–Al<sub>2</sub>O<sub>3</sub> melt mixtures. Selecting and fitting models in a complex system. In: Essential Readings in Light Metals: Volume 2 Aluminum Reduction Technology. Bearne G, Dupuis M, Tarcy G (Eds.). Cham: Springer. 2016. 19–24.
8. Votava I, Matiasovsky K. Measurement of viscosity of fused salts. II. Viscosity of molten binary mixtures on the cryolite basis. Chem Zvesti. 1973;27(5):582–587.
9. Nishihara K, Matsumura Y, Komatsu K, Noguchi H. Suiyokai-shi. 1964;15(6):311–315.
10. Robelin C, Chartrand P. A viscosity model for the (NaF + AlF<sub>3</sub> + CaF<sub>2</sub> + Al<sub>2</sub>O<sub>3</sub>) electrolyte. J Chem Thermodynamics. 2011;43:764–774. doi:[10.1016/J.JCT.2010.12.017](https://doi.org/10.1016/J.JCT.2010.12.017).
11. Bale CW, Bélisle E, Chartrand P, Decterov SA, Eriksson G, Hack K. CALPHAD: Comput. Coupling Phase Diagrams Thermochem. 2009;33(2):295–311. doi:[10.1016/j.calphad.2016.05.002](https://doi.org/10.1016/j.calphad.2016.05.002)
12. Korenko M, Vaskova Z, Priscak J. Density, viscosity and electrical conductivity of the molten cryolite electrolytes (Na<sub>3</sub>AlF<sub>6</sub>–SiO<sub>2</sub>) for solar grade silicon (Si-SoG) electrowinning. Silicon. 2015;7:261–267. doi:[10.1007/s12633-014-9214-2](https://doi.org/10.1007/s12633-014-9214-2)
13. Shramm G. Osnovy prakticheskoy reologii i reometrii [Fundamentals of practical rheology and rheometry] Moscow: KolosS; 2003. 312 p. Russian.
14. Solheim A, Rolseth S, Skybakmoen E. Liquidus temperatures for primary crystallization of cryolite in molten salt systems of interest for aluminum electrolysis. Metallurgical and Materials Transactions B. 1996;27B:739–745.
15. Fellner P, Silny A. Viscosity of sodium cryolite-aluminum fluoride-lithium fluoridemelt mixtures. Berichte der Bunsengesellschaft für physikalische Chemie. 1994;98:935–937.